

High-speed ditching of double curvature specimens with cavitation and ventilation

Emanuele Spinosa, Silvano Grizzi, Alessandro Iafrati
CNR-INM (Institute of Marine Engineering), Rome (Italy)
email address: emanuele.spinosa@cnr.it

September 3, 2025

Abstract

The water entry at high horizontal speed of double-curvature specimens, representing the rear part of the fuselage that first contacts the water during aircraft ditching, is investigated experimentally. Three shapes, reproducing different aircraft types, are analysed through pressure and load measurements, supported by underwater high-speed visualizations. Tests are performed at different horizontal speeds and pitch angles, while maintaining a constant vertical-to-horizontal velocity ratio. The longitudinal curvature is found to significantly affect the hydrodynamics, potentially leading to cavitation and ventilation at the rear at high speeds. The transverse curvature influences pressures and loads at both the front and rear, with higher transverse curvature favouring lateral fluid escape. Higher pitch angles increase loading in both magnitude and distribution. Increasing the horizontal speed results in higher loads at the front and alters cavitation and ventilation modalities at the rear. Load scaling laws established for flat plates are valid at the front but are invalidated at the rear due to cavitation and ventilation. The time evolution of the cavitation and wetted area is analysed through advanced image processing and pressure data. Comparison with the geometric intersection area between the specimen and the still water level offers further insight into the water entry hydrodynamics.

© 2024. This manuscript version is made available under the CC-BY-NC-ND 4.0 license <http://creativecommons.org/licenses/by-nc-nd/4.0/>

1 Introduction

Aircraft ditching is the manoeuvre performed when the pilots and crew are forced to recur to an emergency water landing due to exceptional circumstances such as engine failure, fuel exhaustion, severe weather or other critical unexpected situations. The goal of ditching is to land the aircraft safely on the water surface, allowing the occupants to be evacuated and rescued with the lowest risk of injury. Although being a rare event, airworthiness regulations require a precise certification for ditching, including demonstration tests proving that the aircraft structural damage during this eventuality is limited and that a sufficient floating time is guaranteed for a safe evacuation of the occupants, as specified in European Union Aviation Safety Agency (2020) and Federal Aviation Administration (2023) (see also Desjardins et al. (1989)).

The theoretical foundations of ditching were laid by Von Karman (1929) and Wagner (1932), which first established a theoretical framework of vertical water entry. These initial (semi)-analytical models were successively refined by several researchers (Logvinovich, 1969; Scolan and Korobkin, 2001; Korobkin and Scolan, 2006; Korobkin, 2004; Tassin et al., 2010). forming

the basis of *low-fidelity numerical approaches*, which became popular in the early computational era. A notable example is the Boundary Element Method (BEM) (Zhao and Faltinsen, 1993; Battistin and Iafrati, 2003; Iafrati and Korobkin, 2004, 2008), based on potential theory. Owing to their simplified discretization and rapid computation, these methods are still used today for quick, approximate solutions.

To extend vertical entry solutions to the ditching case, where a significant horizontal velocity is also present, the multi-section or the 2D+t approach can be used (Fontaine and Tulin, 1998), which break down the 3D motion into a series of simpler 2D cross-section analyses (Sun and Faltinsen, 2011), albeit with some limitations. The application of a multi-section approach to aircraft ditching is presented in Del Buono et al. (2021); Del Buono and Iafrati (2025). The DITCH code (Bensch et al., 2003; Streckwall et al., 2007) implements a 2D+t method, complemented by empirical formulations and has also been recently used with machine learning to predict ditching loads (Schwarz et al., 2025).

As computing power increased, *high-fidelity* methods using finer discretization of the Navier–Stokes equations were increasingly employed. Early high-fidelity tools are reviewed in Seddon and Moatamedi (2006) and Hughes et al. (2013). These methods often combine fluid dynamics solvers with structural models, like Finite Element Methods (FEM), for fluid–structure interaction. A common approach uses URANS solvers with Volume-Of-Fluid (VOF) to capture the free surface evolution. This method is applied to aircraft ditching in (Guo et al., 2013; Qu et al., 2015, 2016; Wang, 2023; Zheng et al., 2021, 2025). Free surface evolution can also be captured using over-set approaches (Zha et al., 2024; Song et al., 2023) and Spinosa et al. (2022), the latter focusing on the final phase of ditching after water impact. The ALE method overcomes mesh deformation in Lagrangian methods via periodic re-meshing (Cheng et al., 2011; Siemann and Langrand, 2017; Bisagni and Pigazzini, 2018; Feng et al., 2020; Fan et al., 2024). The CEL method uses a fixed Eulerian mesh for fluids and a moving Lagrangian mesh for solids, to model fluid–structure interaction (Goron et al., 2023, 2025). Mesh-free methods like Smoothed Particle Hydrodynamics (SPH) avoid mesh distortion and capture sprays well. However, they require higher computational resources and still face challenges in modelling cavitation during ditching (Anghileri et al., 2011, 2014; Groenenboom and Cartwright, 2010; Groenenboom and Siemann, 2015; Siemann and Langrand, 2017; Siemann et al., 2018; Bisagni and Pigazzini, 2018; Groenenboom et al., 2021; Muñoz et al., 2025; Wang et al., 2024). Undoubtedly, numerical simulations of ditching have advanced significantly. However, their use in ditching certification remains limited due to high computational costs and the need for rigorous validation against experimental data.

Experimental investigations enable an accurate replication of the physical phenomena in a ditching event and are essential for validating the various computational tools. However, full-scale tests of an entire aircraft remain impractical and prohibitively expensive. Attempts to replicate ditching through scaled-model experiments began in the 1950s with pioneering work by Smiley (1951), who tested flat plates entering water at significant horizontal speeds, obtaining accurate measurements of pressures, loads, and wetted areas under various conditions. While remarkable for its time, the study had limitations, particularly a data sampling frequency of around 1 kHz, insufficient to capture the rapid transients typical of water entry problems. Another notable experimental ditching campaign from the same period was conducted by McBride and Fisher (1953), who performed free-fall tests on various scaled fuselage models representing different aircraft types. The study primarily examined the effects of longitudinal and transverse body curvatures on ditching dynamics. Its main limitation was the inability to control impact conditions. A review of early experimental ditching activities is provided by Smith et al. (1957), while more recent developments are covered in Seddon and Moatamedi (2006); Abrate (2011). More recent scaled model tests of a full aircraft model were presented in Climent et al. (2006); Zhang et al. (2012); Song et al. (2023); Wenli et al. (2025).

The process of scaling aircraft ditching tests from full to model scale presents substantial challenges. In ship hydrodynamics, towing tank experiments often rely on Froude similarity, which ensures correct scaling of the ratio between inertial and gravitational forces. When Froude scaling is applied, the model test speed decreases proportionally to the square root of the scale factor. In the hydrodynamics of water entry, the Reynolds number, representing the ratio of inertial to viscous forces, should also be considered, however, previous studies have shown that viscous effects are negligible (Facci et al., 2015; Moghisi and Squire, 1981). Aircraft ditching involves high horizontal velocities and large-scale impact phenomena, which generate extremely high pressures in some regions of the wetted surface and very low pressures in others. Under these conditions, suction, cavitation and ventilation are likely to occur Hughes et al. (2013); Climent et al. (2006); Zhang et al. (2012); Tassin et al. (2013). Therefore, achieving similarity in terms of cavitation and ventilation numbers is essential (Brennen, 2014). This type of similarity can only be reproduced through testing in a de-pressurized environment or by reaching sufficiently high speeds.

To address these challenges, the High-Speed Ditching Facility (HSDF) at the CNR- Institute of Marine Engineering was designed and built. The HSDF allows tests at horizontal speeds of up to 48 m/s, with vertical-to-horizontal velocity ratios between 0.03 and 0.05, using models approximately 0.7 m wide and 1.3 m long. This setup enables near full-scale hydrodynamic conditions and allows observation of phenomena such as cavitation and ventilation, which cannot be captured at lower speeds or smaller scales. Pressures and loads can be acquired at high sampling rates through an integrated on-board measurement system, while high-speed underwater imaging provides complementary insight into the flow phenomena (Iafrati et al., 2015).

Early tests were performed on a flat aluminium plates, 15 mm thick, in a configuration similar to that used in Smiley (1951). Different test conditions were examined by varying the horizontal speed, the vertical-to-horizontal velocity ratio and the pitch angle. The strong correlation between the spray root propagation velocity and the intensity of the pressure peak was confirmed and a scaling of the total loading with respect to the impacting velocity relative to the body was observed (Iafrati, 2015, 2016). The high speeds achievable also allow for a more accurate investigation of fluid–structure interaction on thin aluminium plates (3 mm and 0.8 mm thick). Experimental results showed that hydrodynamic loads can increase by up to 30% in the presence of significant structural deformation. As a result, load estimates based on tests with rigid specimens may not always be conservative (Spinoso and Iafrati, 2021).

Flat plate tests provided validation data for ditching models. However, the curved geometry of the fuselage lower section required further investigation. Transverse curvature effects were examined using 15 mm thick concave and convex plates (Iafrati, 2018). Furthermore, the longitudinal curvature of the fuselage rear portion induces suction forces due to negative pressures, significantly influencing the aircraft ditching dynamics, as demonstrated by numerical and experimental studies (Climent et al., 2006; Zhang et al., 2012). To elucidate this phenomenon, an experimental campaign was conducted on rigid specimens exhibiting double curvature. From a preliminary analysis of the data it was found that cavitation and ventilation may occur at high speed and they may have important effects on the magnitude and distribution of the loading (Iafrati and Grizzi, 2019; Iafrati et al., 2020).

This paper presents additional results from this extensive experimental campaign. Continuing our past research, we further explore the influence of horizontal speed and offer considerations on cavitation modalities and cavitation number. A key objective of this paper is also to investigate the effects of pitch angle and the longitudinal and transverse curvatures, aspects not addressed in previous studies. Analysis of pressures and total loads on the impacting specimens reveals significant effects at the front and rear, linked to cavitation and ventilation phenomena. Additionally, the temporal evolution of the wetted area and cavitation zone is

examined through underwater visualizations, with quantitative estimates provided. The complexity of the underlying physics often results in theoretical and numerical models exhibiting limited accuracy, especially at high speeds. This paper offers a physical interpretation alongside a comprehensive database to support the validation of these models.

2 Experimental Set-up

2.1 The High-Speed Ditching Facility

The experiments are performed in the High Speed Ditching Facility (HSDF) of the CNR - Institute of Marine Engineering, described in detail in Iafrati et al. (2015). For the purpose of the present paper, it is worth recalling the most relevant features.

The facility is composed of a guide along which a properly designed trolley can freely move. The guide is about 64 m long and it is suspended by five bridges over the CNR-INM towing tank. The guide can be set at different inclinations with respect to the still water level of the basin, thus yielding different vertical-to-horizontal velocity ratios, in the range of 0.03 to 0.05.

The trolley carries a waterproof box that hosts a ruggedized case, with the acquisition system inside. The specimens to be tested are directly connected to the the bottom of the trolley. The trolley is accelerated by a system of eight bungee cords, set in a V-shaped configuration, but it is left to move freely along the guide shortly before the impact of the specimen with the water. Hence, the hydrodynamic loads acting on the model and the constraint forces that the trolley wheels exert on the guide are the only forces acting on the system, since gravity can be considered negligible. The total mass of the trolley and acquisition box is about 900 kg, which is large enough to ensure that the horizontal velocity remains nearly constant during the impact, being the velocity reduction during the impact phase lower than 5% of the initial velocity.

A video showing the execution of one of the experiments can be found at the link <https://www.youtube.com/watch?v=1j5-Z96NNyQ>.

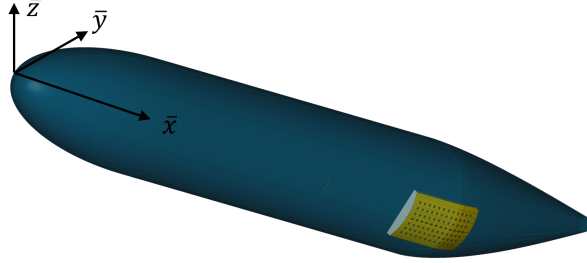
2.2 Specimen shapes

The tested models are double curvature specimens that reproduce the part of the fuselage body that first gets in contact with water during ditching. Just to give an idea, the typical shape of the specimen is the yellow portion of the entire fuselage shown in Figure 1. Three fuselage shapes are considered, denoted here as **S1B**, **S2** and **S3**, which are described in a fully analytical form in Iafrati et al. (2020). For the readers' convenience the details of the analytical formulation are also provided in the following.

The shapes are defined in terms of a few non-dimensional parameters, namely, Length-to-Breadth ratio (L_B), Front length-to-Breadth ratio (F_B) and Rear length-to-Breadth ratio (R_B), where B , the maximum breath of the fuselage, is assumed as the reference length value. Hence, non-dimensional coordinates are introduced as: $\xi = \bar{x}/B$, $\eta = \bar{y}/B$ and $\zeta = \bar{z}/B$ (Figure 2). All shapes are defined by a central region with a constant circular cross-section: a fore part where the circular cross-sections are uniformly and progressively reduced about the centre of the circle until the nose, and a rear part where the shape is shrunk, with the centre of the circle shifted in the longitudinal plane in a way that the upper points are always located at $\zeta = 0.5$. The shapes **S1B** and **S2** have both a circular cross-section whose radius $\hat{r}(\xi)$ varies with the



(a) Side View



(b) 3D View

Figure 1: Drawing of the whole fuselage **S2** (blue) and of the extracted specimen part (yellow) in (a) side view and (b) 3D view. The local coordinate system $(\bar{x}, \bar{y}, \bar{z})$ is also shown.

longitudinal coordinate ξ as follows:

$$\hat{r}(\xi) = \begin{cases} 0.5 \sqrt{1 - \left(\frac{\xi - F_B}{F_B}\right)^2} & 0 < \xi < F_B \\ 0.5 & F_B < \xi < (L_B - R_B) \\ 0.5 + \hat{o}_C(\xi) & (L_B - R_B) < \xi < L_B \end{cases} \quad (1)$$

where the offset function $\hat{o}_c(x)$ is defined as

$$\hat{o}_C(\xi) = -0.5 \sin\left(\frac{\xi - (L_B - R_B)}{K R_B}\right) \cdot \left[\frac{\xi - (L_B - R_B)}{\sin(1/i) R_B}\right]^{1/i} \quad (2)$$

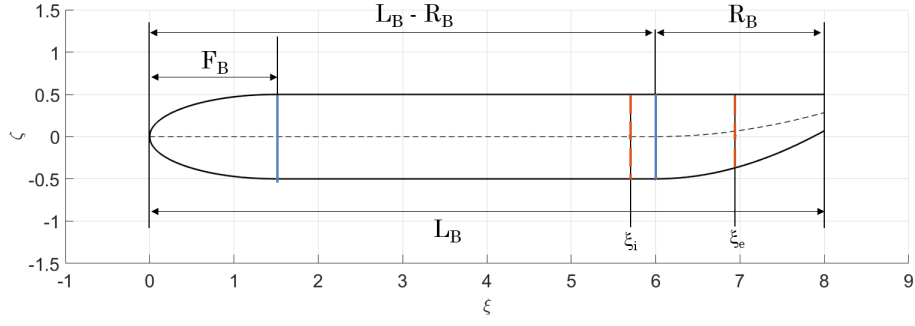
i being a non-dimensional parameter. The centre of the cross-section is located at $\mathbf{O} \equiv (\xi, 0, 0)$ for $\xi \leq (L_B - R_B)$ and at $\mathbf{O} \equiv (\xi, 0, \hat{o}_C(\xi))$ for $\xi > (L_B - R_B)$, thus ensuring that the sections are all aligned at $\zeta = 0.5$ in the rear fuselage portion.

The shape **S3** has a circular cross-section blended with an elliptical cross-section at the bottom. Starting from the circular profile, the elliptical portion is defined by two parameters, i.e the angle θ and the ratio c/h of the shorter ellipse semi-axes to the offset h , see Figure 2(c). The contact and the tangency between the circumference and the ellipse are enforced at the contact points M and N , by choosing the two semi-axes a and c as:

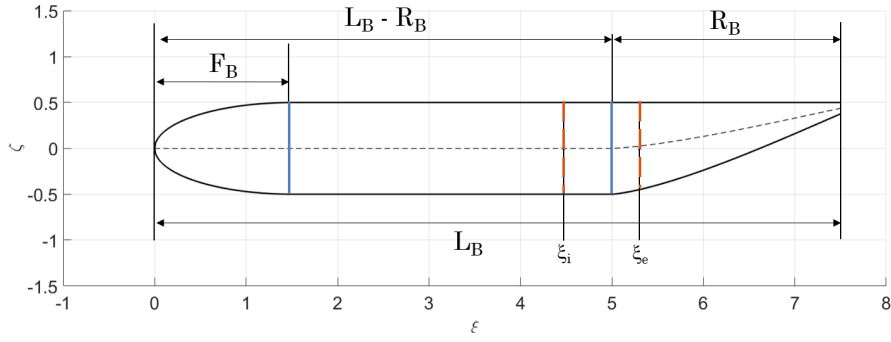
$$a = \frac{c}{h} \frac{\sin \theta}{\sqrt{\left(\frac{c}{h}\right)^2 - 1}} \quad c = \frac{a \tan \theta}{\sqrt{\left(\frac{c}{h}\right)^2 - 1}}, \quad (3)$$

and therefore the bottom part of the section is described by the equation

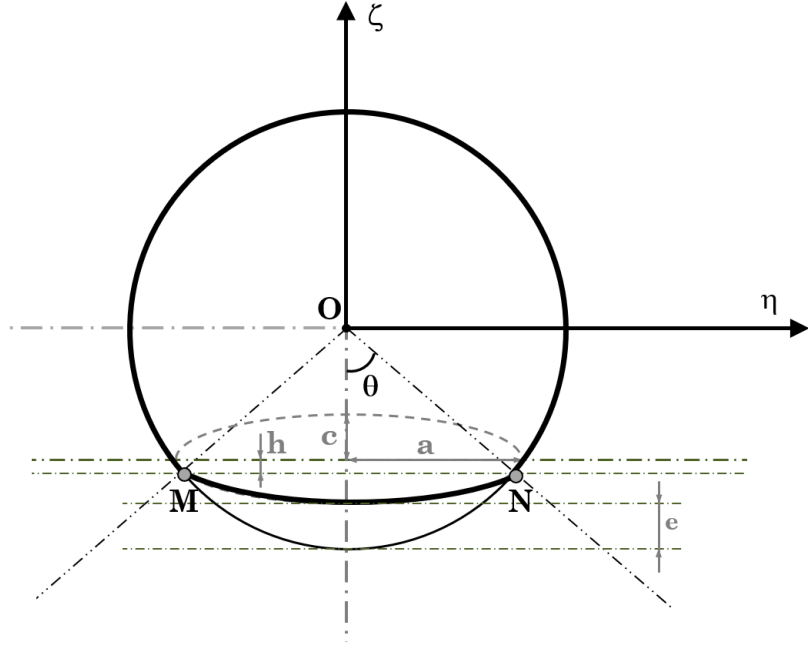
$$\left(\frac{\eta}{a}\right)^2 + \left(\frac{\zeta + 1 - (e + c)}{c}\right)^2 = 1, \quad (4)$$



(a) Midplane section of **S1B**



(b) Midplane section of **S2** and **S3**



(c) Circular-elliptical cross-section of **S3**

Figure 2: Non-dimensional mid-plane sections of the fuselages **S1B** (a) and **S2/S3** (b), where $\xi_i = \bar{x}_i/B$ and $\xi_e = \bar{x}_e/B$, see Table 1. In (c) the construction of the semi-elliptical cross-section of the shape **S3** is sketched.

Parameter	S1B	S2	S3
L_B [-]	8	7.5	7.5
F_B [-]	1.5	1.5	1.5
R_B [-]	2	2.5	2.5
K [-]	2	1.55	2.55
i [-]	1	2.6	2.6
C/H [-]	-	-	5
θ [°]	-	-	50
B [m]	1	1.5	1.5
\bar{x}_I [m]	5.7	6.71	6.71
\bar{x}_E [m]	6.94	7.95	7.95

Table 1: Parameters defining the whole fuselage shapes and the extracted specimens

where

$$e = 1 - \cos \theta - c (1 - h/c) . \quad (5)$$

When the circular-elliptical section is used, the equation of the offset is modified as

$$\hat{o}_{CE}(\xi) = 2\hat{o}_C(\xi)/e. \quad (6)$$

which ensure that the bottom profiles of shape **S2** and **S3** are perfectly overlapped.

The parameters that define the three fuselage shapes are listed in Table 1. Therein, the dimensional parameters \bar{x}_I and \bar{x}_E defining the limits of the specimen in the longitudinal direction are also provided. Note that in all cases the specimens are 1.24 m long and 0.66 m wide. It is worth noting that the specimen **S1B** is extracted from a fuselage with a breadth (diameter) of 1 m, whereas the fuselage **S2** and **S3** from a fuselage with a breadth (diameter) of 1.5 m. The different choice of the was motivated by the need of maximizing, in the case of the specimen **S1B**, the vertical distance between the lowest point, i.e. the first contact point, and the leading edge of the specimen, which defines the time at which the front of the specimen gets below the still water level and thus the end of the impact phase.

The difference among the three shapes, set at a pitch angle of 6°, is highlighted in 3(c), in which a three-dimensional view is shown, whereas the longitudinal and transverse sections passing through the point of first contact with water, are shown on 3(a) and (b) respectively.

For the experimental data analysis two reference frames are defined: a *ground fixed reference frame* and a *trolley-fixed (or specimen-fixed) reference frame*, both shown in Figure 4. The coordinates associated with the ground-fixed reference frame are indicated with upper-case letters X , Y and Z . In particular, X is parallel to the undisturbed free surface, Z is vertical and directed upwards and Y is in the direction on a right-handed coordinate system. The specimen horizontal and vertical speed are defined in this reference frame as $U = dX/dt$ and $V = -dZ/dt$, respectively. The coordinates associated with the trolley-fixed reference frame are indicated with lower-case letters x , y and z , with origin **O**. As shown in Figure 4 the origin is located at the leading edge of the plate. The x coordinate is parallel to the longitudinal axis of the trolley, the z -coordinate is normal to it and directed upwards, whereas the y axis forms and right-handed coordinate system. The pitch angle α is defined as the angle between the trolley axis x and the X -direction, whereas the angle $\beta = \arctan V/U$ is introduced to denote the angle between the the impact trajectory of the specimen and the undisturbed water level.

For each shape, at given α and β , it is worth defining the point **C** as that where the longitudinal curvature starts changing at the rear, which is the point with dimensional x -coordinate $(L_B - R_B)$ in Figure 2(a,b), and the point **H**, which defines the lowest point of the specimen, and thus the first getting in contact with water. As it is possible to see, the two

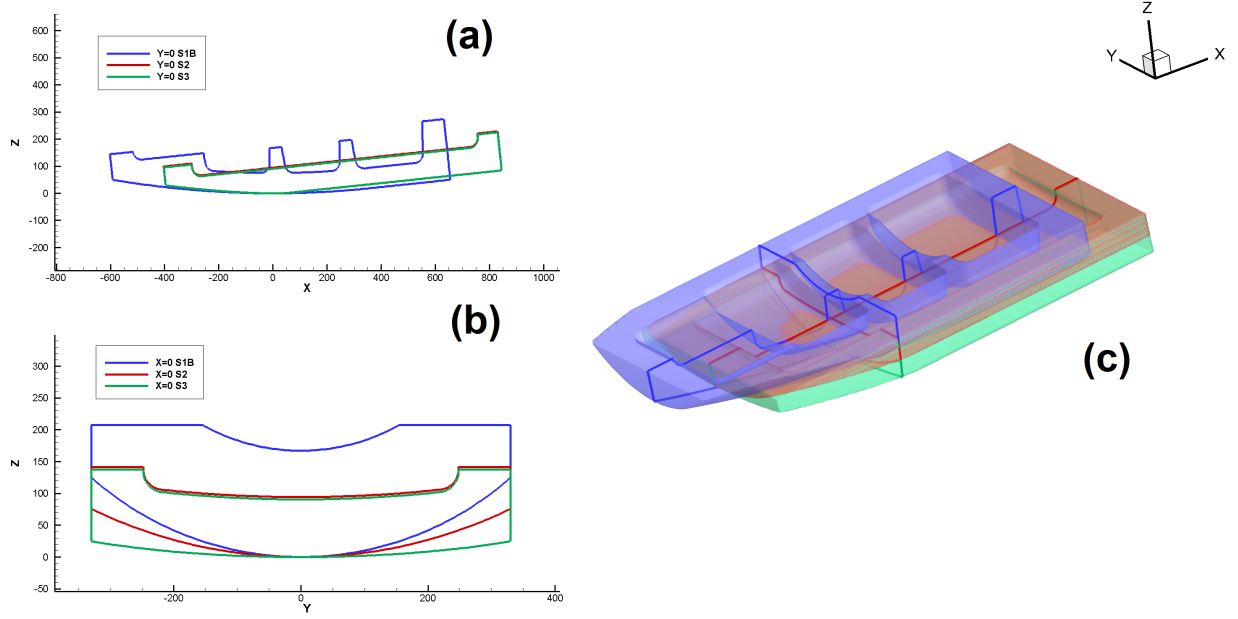


Figure 3: Comparison among the geometry of the three specimens aligned with respect to the lowest Z point, i.e the point of first contact with water: (a) section on the longitudinal plane (b) section on the transverse plane and (c) 3D view

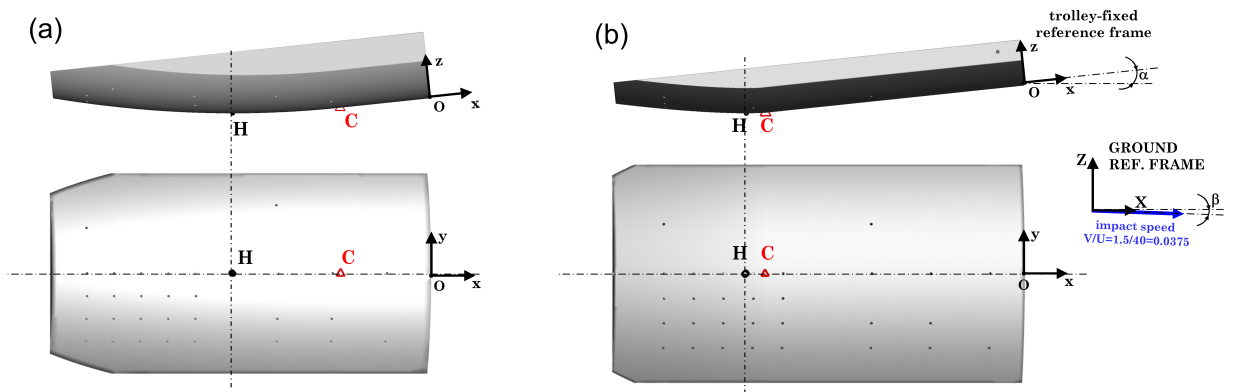


Figure 4: Reference frames, coordinate systems and points of interest to study the water entry of the shapes **S1B** (a) and **S2/S3** (b) at a pitch angle of $\alpha = 6^\circ$.

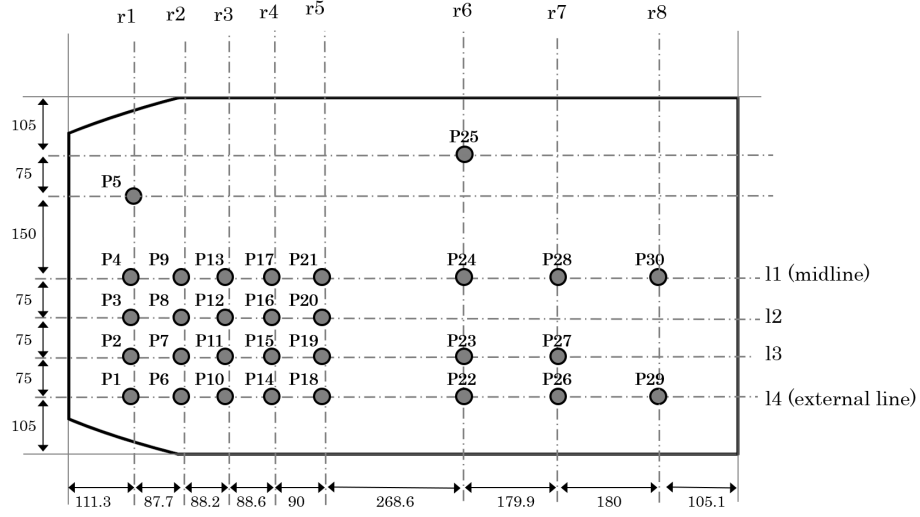
points are very close to each other for the fuselage shapes **S2** and **S3** and relatively far in case of shape **S1B**.

2.3 On-board Measurements

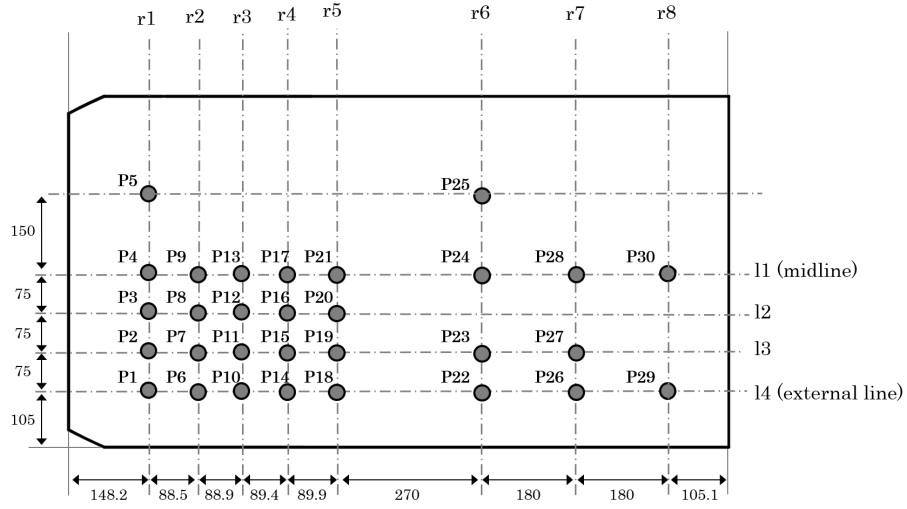
Pressures are acquired through thirty pressure probes type Kulite XTL 123B, full scale range of 300 psi. The probes were carefully calibrated by the manufacturer prior to delivery and were subsequently re-calibrated for verification in the metrology laboratory of CNR-INM before installation. It was found that the sensitivity values were, in all cases, very close to those provided by the manufacturer, with a discrepancy of approximately 1%. Following standard procedures, the relative expanded uncertainty attributed to random effects was determined to be 1.7% of the average measured pressure at a 95% confidence level and 0.9% at a 67% confidence level. The probe was also tested at a few temperatures within its 0–40 °C compensation range, showing a linear sensitivity of about 0.021 kPa/°C. A typical 5 °C temperature change, experienced as the probes operate between approximately 20 °C and 15 °C, causes a negligible pressure shift of 0.105 kPa (0.0051% of full scale). This drift is expected and does not require any further compensation. The probes are installed flush to the external surface of the specimen with ± 0.1 mm accuracy. The position of the probes is given in Figure 5. In the analysis of the data, beside the specific probe number, reference is also made to probe lines ($l1, l2, l3, l4$) and rows ($r1, r2, \dots, r8$) as indicated in the figures. The pressure time histories presented in the following are raw data, unless otherwise specified. It is worth noting that sometimes pressure spikes of non-physical origin may appear, caused, among other reasons, either by slightly protruding probes generating cavitating vortices at such speeds (Iafrati et al., 2015) or by the temperature shock experienced by the sensors when they are suddenly immersed in water at a lower temperature than air (Van Nuffel et al., 2013). It is important to clarify that the presence of these spikes is not in contradiction with the considerations on temperature sensitivity made above, since they result from sudden temperature shocks, whereas sensitivity tests are performed by manually applying temperature variations, which are consequently much more gradual.

The acquisition box hosting the specimen is connected to the trolley by a total of six single-axis load cells, installed between two floating pins to minimize the loading in other directions, as shown in Figure 6. Four Kistler 9343 cells, with full scale range of 70 kN, are used in the z -direction, whereas two Kistler 9363 cells, with full scale range of 120 kN, are used in the x -direction. The load cell signals are conditioned using a charge amplifier type Kistler 5073-A421. The channels are connected so that the loads acting in the z -direction can be separated into the rear F_{zR} and front F_{zF} contributions, whereas F_x denotes the load acting in the x -direction. The distance H for the three specimens **S1B**, **S2** and **S3** are 520 mm, 440 mm and 436.2 mm respectively. Although the single load cell is very accurate when loaded directly along its axis, the connection to the frame of the acquisition box introduces some uncertainties, since the loading is not exactly aligned with the axes of the cells. Furthermore, due to the inherent free play of the installations, some errors may be expected for low values of the loading. For this reason a careful calibration was carried out before starting the test campaign, and it was found that the recorded data are always below the actual loading. The underestimate ranges from about 8% for a load of order of 1.2 kN and reduces continuously when increasing the load, being about 4% for a load of order of 14 kN. The load was also applied at different locations along the x -axis and the centre of loads could be retrieved with a satisfactory accuracy by the combined data of the rear and the front load cells. Unless specified differently, also the force time histories provided in the following are raw data.

All the data are acquired by a ruggedized acquisition system hosted in the acquisition box. The acquisition system is composed of four Dewesoft[©] Sirius modules and one Dewe43 module. All channels are sampled at 200 kHz with a double level A/D 24 bit conversion.



(a) Shape **S1B**



(b) Shapes **S2** and **S3**

Figure 5: Position of the pressure probes and definition of the row and lines used for the discussion. Dimensions are in mm.

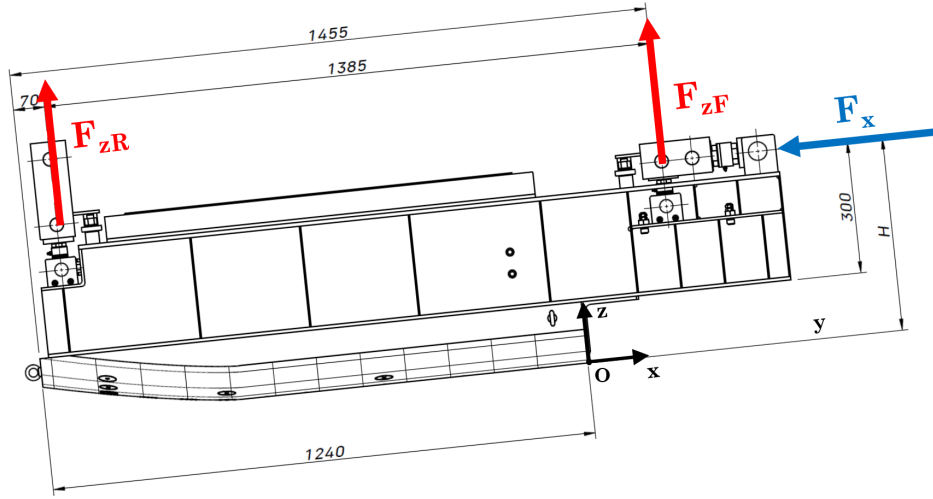


Figure 6: Position of the load cells, referring to the specimen **S2**. The total rear and front force direction is indicated, as well as the trolley-fixed reference frame. The dimensions are in mm. The value of H is 520 mm, 440 mm and 436.2 mm for the shapes **S1B**, **S2** and **S3**, respectively.

The repeatability of the pressure and load measurements was thoroughly investigated by Iafrati et al. (2015) in the context of flat plate tests conducted in the HSDF. These considerations are directly applicable to the present experiments, as the same types of pressure probes, load cells and data acquisition systems were employed. Nevertheless, to verify the experimental repeatability under the current conditions, each test was repeated at least twice. The resulting time histories showed excellent agreement, with only minor discrepancies. These were primarily attributed to the inherent difficulty in precisely reproducing the same target nominal velocity, which led to a small variation of approximately 1%.

2.4 High-Speed Cameras

Two high speed cameras are used to record the tests. One camera, type Photron FastCam Mini AX, operating at 5000 fps, is installed at the side of the facility at the location of the water entry, and it is mainly used to retrieve the horizontal velocity at the exact moment the specimen touches the water. A second camera, type Photron FastCam SA-X2, operating at 3000 fps, is installed on a properly designed waterproof case and positioned underwater. This camera records the water entry from below and provides important information for a more complete interpretation of the hydrodynamic phenomena and of the pressures/loads measurements. Both cameras are synchronized with the on-board acquisition systems.

2.5 Test Conditions

The test conditions that are discussed in the present paper are listed in Table 2. The guide inclination angle is $\beta = \arctan(V/U)$. For all tests examined $V/U = 1.5/40 = 0.0375$, so $\beta = 2.1476^\circ$ (see again Figure 4). It is worth noticing that, due to the use of bungee ropes to accelerate the trolley, a very precise control of the speed cannot be achieved, which is the reason why the actual values of the horizontal speed are not exactly the nominal expected values, also shown in the table. It should be noted that in the discussion from now on, however, reference will be made to the nominal velocity values and not to the actual ones reported in the table.

Water temperature was measured on a near-daily basis using a thermometer. Recorded values ranged from 15 to 18° C. The air temperature was approximately 20° C.

The three groups refer to the test cases examined to investigate the effect of the horizontal

<i>Effect of speed</i>						
Shape	Nominal U	U	V	Pitch	V/U	$(t_E - t_0)$
	[m/s]	[m/s]	[m/s]	[°]	[-]	[s]
S2	30	29.87	1.12	6	0.0375	0.0671
S2	35	34.5	1.29	6	0.0375	0.0515
S2	40	40.25	1.51	6	0.0375	0.0491
S2	45	46.19	1.73	6	0.0375	0.0436
<i>Effect of shape</i>						
Shape	Nominal U	U	V	Pitch	V/U	$(t_E - t_0)$
	[m/s]	[m/s]	[m/s]	[°]	[-]	[s]
S1B	40	40.45	1.52	6	0.0375	0.0260
S2	40	40.25	1.51	6	0.0375	0.0491
S3	40	40.25	1.51	6	0.0375	0.0468
<i>Effect of pitch angle</i>						
Shape	Nominal U	U	V	Pitch	V/U	$(t_E - t_0)$
	[m/s]	[m/s]	[m/s]	[°]	[-]	[s]
S2	40	40.57	1.52	4	0.0375	0.0314
S2	40	40.25	1.51	6	0.0375	0.0491
S2	40	40.08	1.50	8	0.0375	0.0670

Table 2: Test Conditions.

speed, of the shape and of the pitch angle. The test condition highlighted in bold is the one used as a baseline test condition when examining the effects of the above-mentioned parameters.

3 Results and discussion

3.1 Definition of the impact phase

For the purpose of the present study, the data analysis is limited to the *impact phase*, which lasts from the time of first contact of the specimen with the water surface, t_0 , up to the time t_E at which the root of the forward propagating spray reaches the leading edge of the specimen. As done in Iafrati and Grizzi (2019), t_0 can be approximated as the time at which the first pressure probe exhibits a pressure growth, whereas t_E is estimated by linear extrapolation starting from the times at which the pressure peak passes over the location of the probes P28 and P30 (Iafrati, 2016). As shown in Figure 4, for the shapes **S2** and **S3** at a pitch angle of 6° the estimation of t_0 based on the time history of the pressure measured by the probe P17 is expected to be quite accurate, being the probe P17 located very close to the point of first contact **H**. Instead, for the shape **S1B** the first contact point is located between P21 and P24, therefore the estimate of t_0 is more uncertain. The estimate based on pressure measurements is corrected by computing the time duration of the impact phase from the underwater videos and subtracting it from t_E .

It is important to note that tests conducted on specimens can effectively capture the hydrodynamic behaviour of the entire fuselage ditching (with the imposed trajectory, horizontal speed, and constant pitch angle), as long as the wetted area during water entry remains within the specimen's boundaries. This definition of the impact phase ensures that the forward part of the wetted area stays within the specimen's area until it reaches the leading edge. Since the front and rear walls are located above the specimen's profile, they do not affect the pressures underneath, at least until the impact phase ends. Minor discrepancies may occur, after the cavitation region or the wetted area reaches the trailing edge or the lateral edges, but these

differences are believed to be small.

Once t_0 and t_E are defined, a non-dimensional time variable, denoted as τ can be defined as

$$\tau \doteq \frac{t - t_0}{t_E - t_0} . \quad (7)$$

The use of the non-dimensional time τ allows a fairer comparison of the results obtained at different test conditions, and, in particular, at different pitch angles.

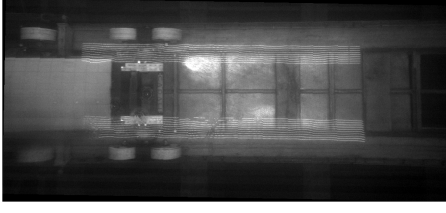
3.2 Hydrodynamics phenomena during the water entry

Qualitative considerations on the hydrodynamics of the water entry of the double curvature specimens can be made through a comparative analysis of the pressure time histories and the underwater high-speed videos. Such an analysis is conducted on the test of the shape **S2**, advancing with a horizontal velocity $U=40$ m/s, velocity ratio $V/U=0.0375$ and pitch angle $\alpha=6^\circ$. Video frames taken at different τ , displaying the flow evolution on the bottom of the specimen, are shown in Figure 7. The time histories of pressure measured by probes located in the same row (see Figure 5 for the row definitions) are shown in Figure 8. From the underwater frames shown in Figure 7 it is possible to recognize the wetted area as the darker region. During the early stage of impact, i.e. in Figure 7(b, c, d), the wetted area grows in all directions. The brighter zone around the wetted area represents the spray region.

In the *front part of the specimen* the spray propagates in a way similar to that observed during the water entry of a curved plate, as shown in Iafrati (2018). The spray root is characterized by a localized pressure peak that causes a sharp rise of the pressure recorded by the probes, as shown in Figure 8 for rows from $r5$ to $r8$. After the passage of the peak, the pressure gradually diminishes, similarly to what found for the flat plates (Iafrati, 2016; Iafrati et al., 2015) or convex plates (Iafrati, 2018). As observed in Iafrati et al. (2015), the pressure drop recorded by some of the probes (see for example P22, P25 or P26) before the sharp pressure rise is associated with the interaction of the flow in the spray tip with the probe itself, which can also induce cavitating vortices. For the probes located at the row $r5$, which for the shape **S2** at 6° pitch is just ahead of the point of first contact, all probes approach a constant negative pressure value, slightly higher than the vapour pressure. From both the underwater images it is possible to see that the spray root is curved backwards, due of the combined action of three-dimensional effects and of the transverse curvature of the specimen, as observed in flat plates (Iafrati, 2016), and in convex plates (Iafrati, 2018), respectively. This is also confirmed by the time histories of the pressures, from which it is observed that the spray root region, i.e. the pressure peak, reaches first the probes located in the mid-line, such as P21, P24, P28 and P30, and next the probes located at the sides, see for instance the recordings of the probes on $r5$ in 8(e) . In Figure 8(d), the time histories of probes P23 and P25, are very close to each other, with the pressure peak exhibiting about the same delay compared to the probe P24, confirming that a satisfactory level of symmetry is achieved.

In the *rear part of the specimen*, i.e. the region behind **C**, the hydrodynamics is quite different from that observed in the front part. In the early stage the wetted area propagates backwards, although at a lower speed than that observed in the front part. This is coherent with the lower the values of the pressure peaks measured by the probes located at the rear, such as P17. Soon after the passage of the spray root, the pressures decrease quite rapidly and become negative. Such a behaviour is associated to the shape of the body and with the impact conditions. A qualitative explanation can be provided from two different points of view, i.e. focusing on the flow in the midplane (longitudinal plane) or on the flow in the transverse plane.

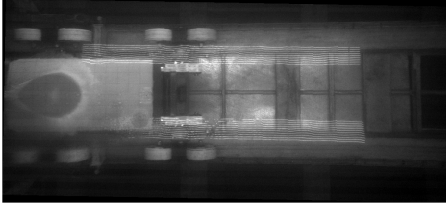
By focusing on the *longitudinal plane* (midplane) in the trolley-fixed reference frame, the results of the two-dimensional case of an asymmetrical wedge entering water with a horizontal



(a) $\tau = 0$



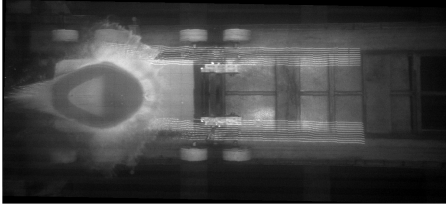
(b) $\tau = 0.1$



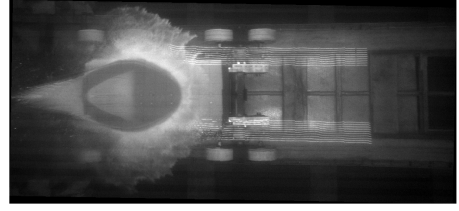
(c) $\tau = 0.2$



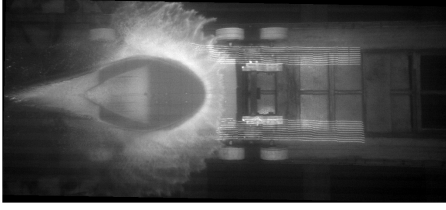
(d) $\tau = 0.3$



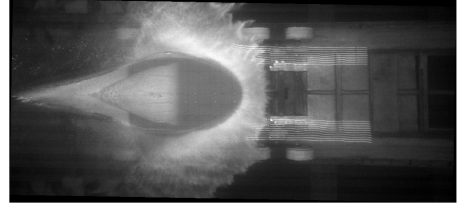
(e) $\tau = 0.4$



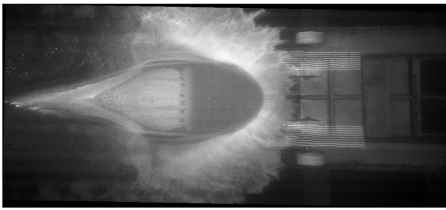
(f) $\tau = 0.5$



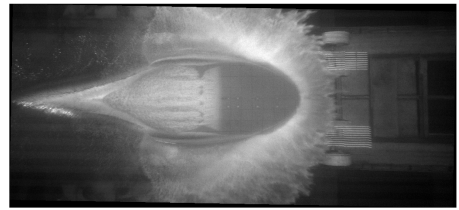
(g) $\tau = 0.6$



(h) $\tau = 0.7$

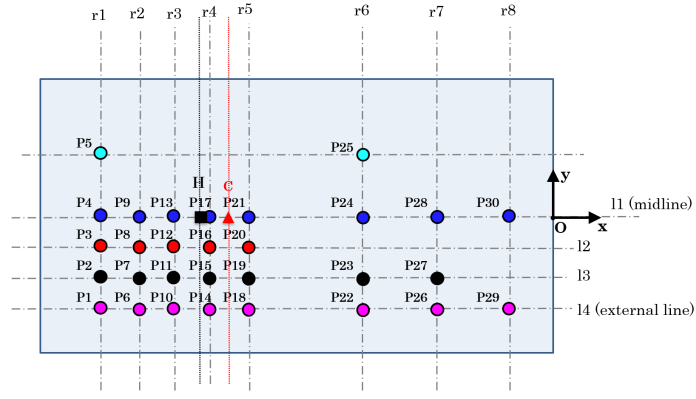


(i) $\tau = 0.8$

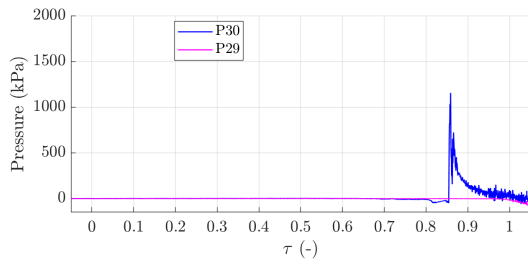


(j) $\tau = 0.9$

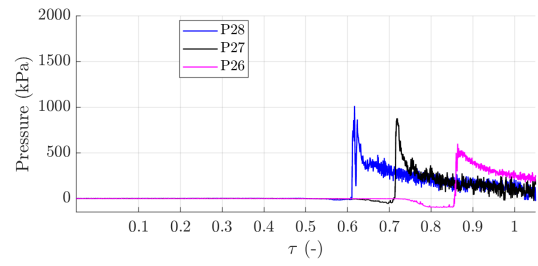
Figure 7: Frames of the underwater video at different τ during the water entry of the shape **S2** at a nominal horizontal speed of $U=40$ m/s and at a pitch angle of $\alpha=6^\circ$. The specimen moves from left to right.



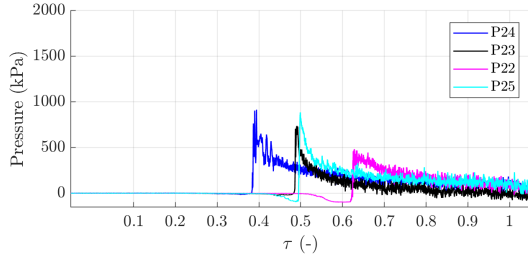
(a) Probe positions: **C** – separation between zero-curvature part on the right and finite-curvature part on the left; **H** – first contact point at $\alpha = 6^\circ$.



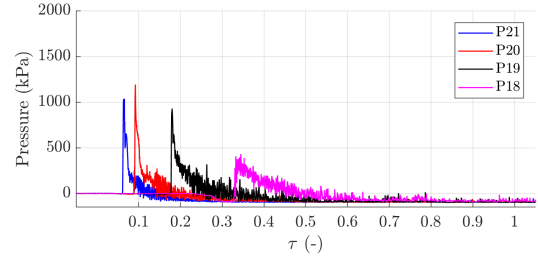
(b) Row $r8$



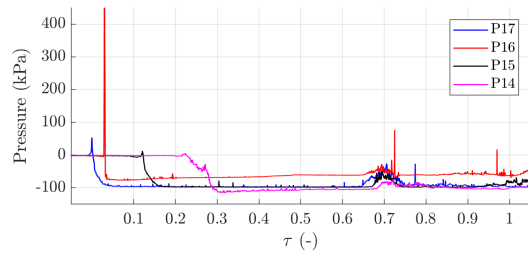
(c) Row $r7$



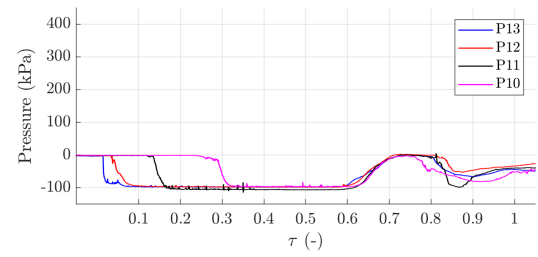
(d) Row $r6$



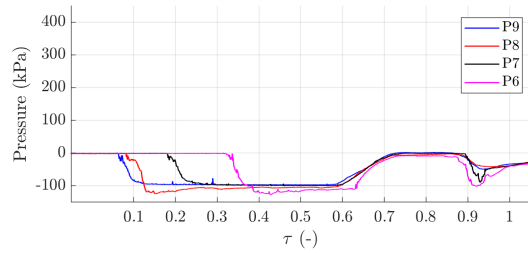
(e) Row $r5$



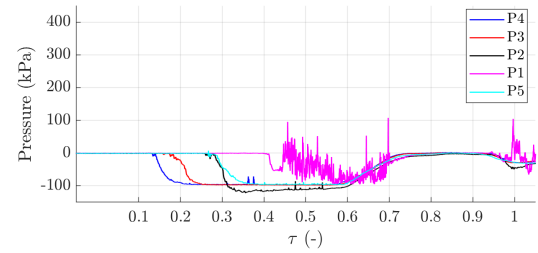
(f) Row $r4$



(g) Row $r3$



(h) Row $r2$



(i) Row $r1$

Figure 8: Pressure probe time histories row by row for the shape **S2** moving at $U=40$ m/s, at a pitch angle of $\alpha=6^\circ$.

velocity (Judge et al., 2004; Xu et al., 2008; Krastev et al., 2018) can provide some elements for the interpretation of the flow phenomena in the present case. In fact, as a consequence of the kinematic asymmetry of the flow due to the horizontal speed, the pressure on the front part of the specimen is higher than that at the rear. From a theoretical standpoint, it is expected that a velocity singularity will occur at the apex (Judge et al., 2004). In real flows, a strong local velocity acceleration is observed there, accompanied by a pressure drop, which is similar to what occurs on the suction side of hydrofoils (Faltinsen, 2005; Newman, 1971). The flow field presents also similarities with that of the vertical water entry of inclined asymmetric wedges (Semenov and Iafrati, 2006; Riccardi and Iafrati, 2004). In Xu et al. (2008), in which a wedge entering water with both a vertical and a horizontal velocity is studied using a self-similar approach, even if the velocity ratio U/V is much lower than the present case, a local pressure drop to negative values is observed at the wedge apex.

An alternative interpretation of the pressure behaviour can be obtained by focusing on the flow in the *transverse plane*, in an earth-fixed reference frame, by exploiting the so called 2D+ t approach (Fontaine and Tulin, 1998; Iafrati and Broglia, 2010). In the front part the plate always penetrates into the water, whereas in the rear part, depending on the local inclination of the tangent to the body surface in the longitudinal plane and on the U/V velocity ratio, the fluid flow problem changes from a water entry to a water exit one (Tassin et al., 2013) and when this happens, negative pressures develop. The development of low and even negative pressures occurs very shortly after the first contact with water and, based on the above considerations, the pressure drop is expected to be higher if the gradient in the slope of the body surface is more significant, which means in presence of larger longitudinal curvature.

The simulations of the horizontal planing motion of the same scaled fuselage models at low speeds and at the same pitch angle, discussed in Spinosa et al. (2022), may also offer insight on the hydrodynamics of the water entry at high horizontal speed. This work also demonstrates the attainment of negative pressure behind point **H**. Furthermore, it is shown that the pressure does not become negative abruptly at point **H**. Instead, the low pressure region extends slightly ahead of this point.

As observed in Iafrati and Grizzi (2019), the pressure drop can be so high that the vapour pressure value may be reached. With a water temperature between 15 and 18 ° C, the vapour pressure relative to the atmospheric value, denoted as p_{vap} , is in the range -99.6 and -99.2 kPa. This explains the formation of a cavitation region (Acosta, 1973; Wang et al., 2001; Brennen, 2014), as shown in the underwater images of Figure 7 at the non-dimensional time $\tau \geq 0.2$. In the trolley-fixed reference frame, the cavitation region has a sort of reverse "D" shape, which follows the pressure distribution on the bottom of the specimen. As the specimen enters in water, the forward front of the cavitation region maintains rather straight and located about the point of curvature change **C**, whereas the rear edge of the cavitation region spreads backwards towards the trailing edge of the specimen. Once the cavitation region reaches the trailing edge of the specimen, the water vapour inside it, at vapour pressure, comes into contact with air at atmospheric pressure. As a consequence, air is suddenly entrained into the water vapour cavity, forming a *ventilation zone* that expands in the opposite direction, i.e. towards the leading edge. This behaviour is typical of the so called *cavitation-ventilation regime*, described in more detail in Section 3.3 based on the analysis of the water entry of the specimen **S3** (Iafrati and Grizzi, 2019; Iafrati et al., 2020) and also occurs for **S2** at the same horizontal speed.

The expansion of the cavitation region can be also recognized by observing the time histories of the pressure probes, see Figure 8. The passage of the rear edge of the cavitation region corresponds to the abrupt drops to the vapour pressure value. Moving backwards, i.e. from row $r4$ to row $r1$, the instant at which the drops occur for the midline probes (P17, P13, P9 and P4) increases. This time delay is related to the propagation velocity of the rear edge of the cavitation region. Comparing the pressure time histories across the same rows, it can be noted

that pressure drops of the midline probes are delayed with respect to those of the probes at the sides, due to the combined effect of the body shape and of the curvature of the rear edge of the cavitation region. When ventilation starts and air is entrained within the cavity, pressures start increasing progressively, reaching the zero-pressure value. It is worth noting that, in contrast to the pressure drop associated with the propagation of the cavitation region, the rise in pressure values during this phase is gradual and occurs at extremely close time instants for all pressure probes positioned on the same row. The increase in pressure values occurs later in time, when progressing from row $r1$ to $r4$. This clearly indicates that the ventilation front is advancing at an extremely high speed, as previously observed for the shape **S3** in Iafrati and Grizzi (2019).

A comprehensive global overview of the shape and evolution of the cavitation region can be derived by constructing pressure iso-lines using the available pressure data from row $r1$ to $r5$ at different time instants. In Figure 9, iso-lines are superimposed on the corresponding video frames at $\tau = 0.3$, $\tau = 0.6$, and from $\tau = 0.7$ to $\tau = 0.8$ with a finer non-dimensional time resolution of $\Delta\tau = 0.02$. Although the probe spacing is not fine enough to provide a very accurate interpolation, especially in this case where relevant pressure gradients are present, it is evident that after the first contact with water, the pressure iso-lines also assume the shape of a reverse D and expand in time in the interval between $\tau = 0.3$ and $\tau = 0.6$. The pressure values in time decreases overall and from a certain τ reach the value of p_{vap} within the inner iso-line, which matches the shape of the cavitation region visible in the video frames. As the cavitation region reaches the trailing edge, the ventilation front starts moving back very fast towards the leading edge. The ventilation front is visible especially at $\tau = 0.8$, where the iso-lines at $p \approx 0$ have advanced towards the leading edge, having almost reached the point **C**. The ventilation front at this time instant appears to be quite straight in the transverse direction.

Observing the pressure time histories, it can be observed that ventilation occurs within the time interval between $\tau \approx 0.7$ and 0.8 . By focusing the pressure iso-lines over this time interval, as shown in Figure 9, it is possible to gain more insight on the ventilation dynamics. In fact, it is observed that the pressure begins to rise back to the atmospheric value first at the centre, since the cavitation region reaches the trailing edge first there. However, the ventilation front develops rapidly and at about $\tau = 0.78$, becomes roughly parallel to the transverse direction, as also observed for the shape **S3** in Iafrati and Grizzi (2019).

In Figure 10 the normal loads acting on the specimen recorded by the rear and front cells are plotted. The data of two test repeats, denoted as R1 and R2, performed at the same conditions are drawn. The red and blue vertical lines indicate the non-dimensional time at which the cavitation and the ventilation phases start, respectively. These time instants are determined by using the data of the pressure probes: the cavitation phase is assumed to start when the pressure at probe P17 drops to the vapour pressure value, while the ventilation phase when the pressure at probe P4 begins to rise to atmospheric pressure. The time histories of the force components exhibit some oscillations, which are more evident when the loads are low. These oscillations are partly due to the vibrations of the trolley, as it moves along the guide, and partly to the free play at the joints. In spite of these oscillations, the data of the two repeats display a quite similar trend. The loads measured by the front cells are always positive and grow progressively as time elapses, which is consistent with the positive pressures recorded by the probes located from $r5$ to $r8$ (see Figure 6). The load measured by the cells at the rear is rather low at the beginning, which is presumably associated with the development of cavitation, starting slightly before $\tau = 0.1$ at this specific test condition. As the cavitation region expands, the loads measured at the rear undergo a reduction, which is rather evident between $\tau \approx 0.4$ and $\tau \approx 0.6$. As soon as the ventilation starts, the loads at the rear start increasing and turn positive. Such growth is consistent with the increase in the pressure at the rear of the body, when the pressure passes from the vapour pressure value to zero (atmospheric pressure). The

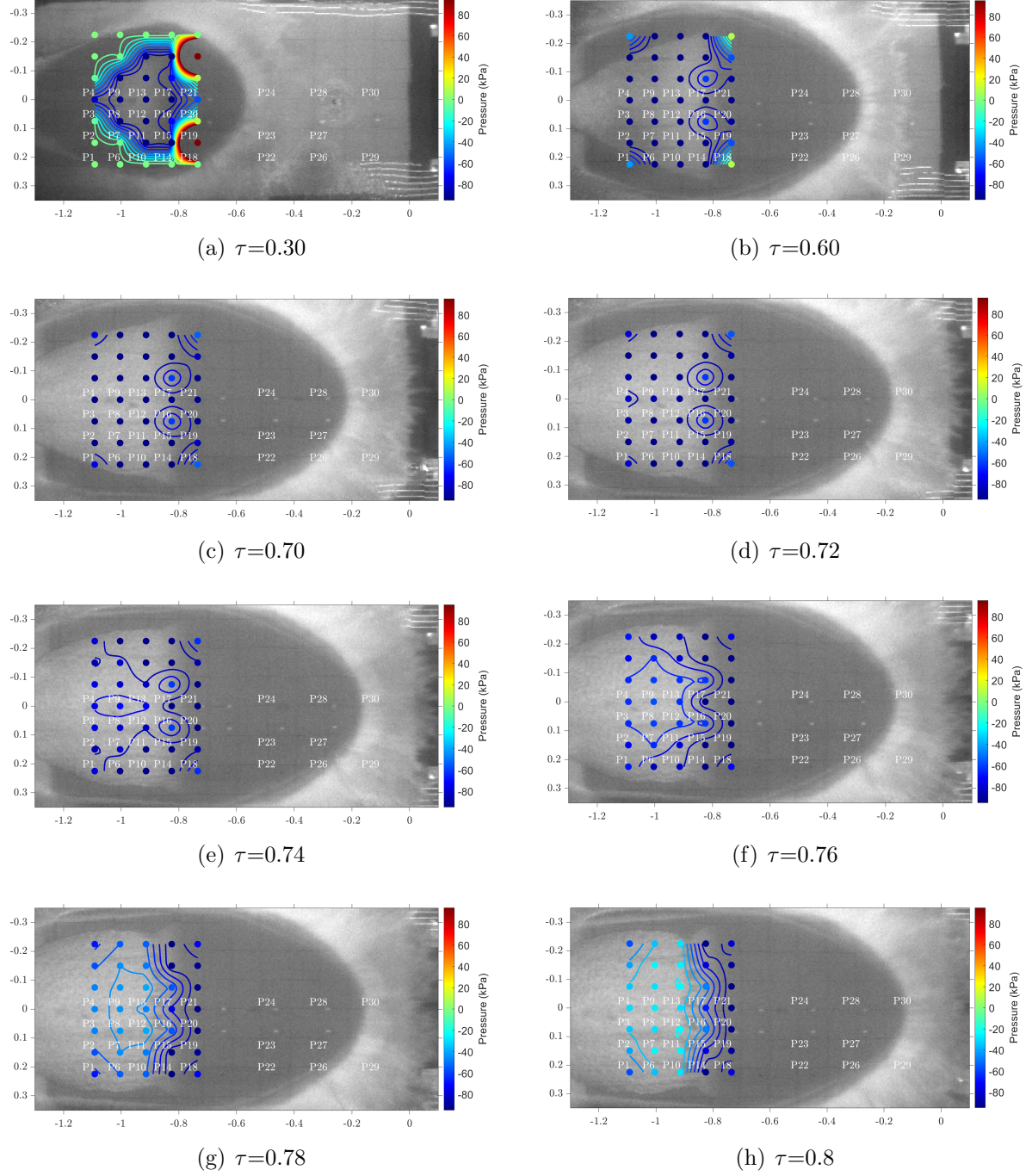


Figure 9: Pressure iso-lines in the rear part of the specimen overlapped to the underwater video frames for the test of shape **S2** at $U=40$ m/s, at $\alpha = 6^\circ$ at the specified τ values. The symmetry about the mid-line is exploited.

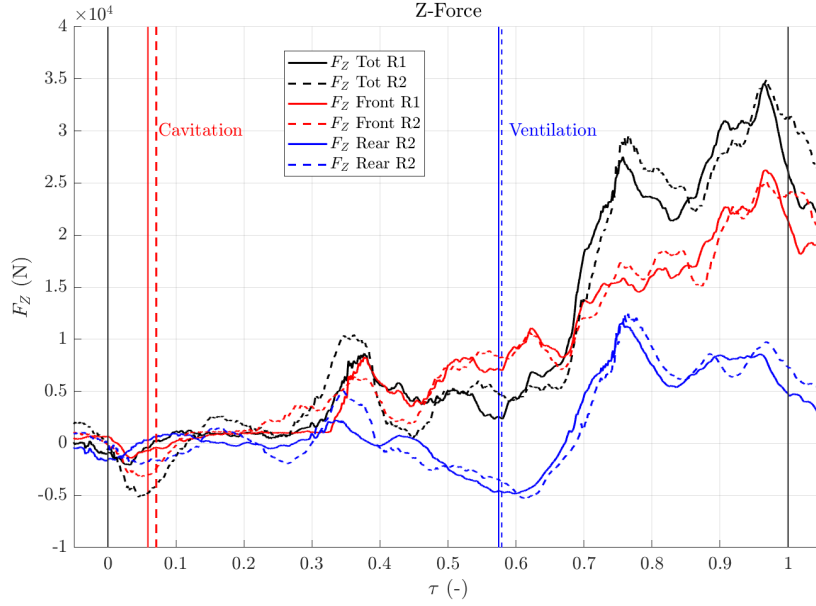


Figure 10: Time histories of the forces recorded by the front (red) and rear (blue) load cells and of the total normal load (black), for shape **S2** at 6° pitch angle and $U=40$ m/s. The vertical red and blue lines indicate the start of cavitation and of ventilation respectively. The solid and dashed lines refer to the first and second test repeat respectively (denoted as R1 and R2).

load at the rear remains almost constant after $\tau \approx 0.8$, whereas the total load continues to grow up to $\tau = 1$, when the spray root has reached the leading edge. At this time the front face of the trolley starts penetrating into the water, circumstance that reduces the horizontal speed and then the loads.

In the next sections, comparisons are established between tests performed at different conditions, in order to evaluate the effect of the horizontal speed, pitch angle and body curvature on pressures and loads.

3.3 Effect of the ditching speed

As previously noted in Iafrati and Grizzi (2019); Iafrati et al. (2020), significant alterations in the hydrodynamics of the water entry are observed when the horizontal speed is varied for the shape **S3**. As shown in Table 2, when the horizontal speed is varied while keeping the ratio V/U constant, the vertical speed also varies. In particular, at least four regimes were identified: a *no-cavitation regime* (for U lower than about 27 m/s), in which no cavitation is observed; an *incipient cavitation regime* (between $U \approx 27$ m/s and 35 m/s) in which a cavitation region expanding in time only up to a certain τ can be seen; an *intermediate regime*, (between $U \approx 35$ m/s and 37 m/s) (denoted in Iafrati and Grizzi (2019) as *Full Cavitation Bubble* and *Cavitation Alternate with Ventilation*), in which the cavitation region reaches the trailing edge, followed by the formation of a local ventilation region, which does not expand in relevant way; finally a *cavitation-ventilation regime* (U higher than 37 m/s), in which the ventilation region exhibits a successive fast expansion towards the leading edge of the specimen.

In the present work, the effect of the horizontal speed is analysed for the shape **S2**, entering water with a pitch angle of 6° and at velocity ratio of $V/U = 0.0375$. The analysis is performed in terms of pressures and loads and through the observation of the underwater images taken at two non-dimensional times, i.e. $\tau = 0.2$ and $\tau = 0.6$. A comparison is presented between the time histories of pressures recorded by the probes located on the midline and on line *l3*.

(Figure 6). In order to make the comparison easier, the probes lying along rows $r5 - r8$ and $r1 - r4$ are plotted in separate graphs. The results for $U=30$ m/s and 35 m/s are shown in Figure 11, whereas those for $U=40$ m/s and 45 m/s in Figure 12.

As shown in Figures 11 and 12 the *probes located in the front*, i.e. ahead of the point **H**, are characterized by the typical sharp rise, followed by a gentle decay. It is worth noting that, for all probes, the non-dimensional time τ at which the pressure peak is attained is almost independent of the horizontal speed, whereas the peak value increases with the speed. As expected, the peaks recorded by the probes along the line $l3$ occur at a later time with respect to the peaks recorded by the probes at the midline in the same row. This is a consequence of the combined effect of the transverse curvature of the specimen and of the curvature of the spray root, which is associated with the possibility for the water to escape from the sides (Iafrati, 2016).

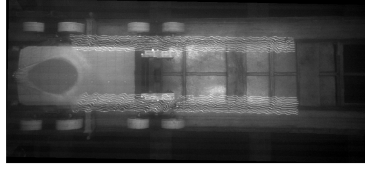
The analysis of the pressure measurements of the *probes located behind the point H* is less straightforward and the support of the underwater images is needed for a correct interpretation. In fact, looking at the underwater frames in Figures 11 and 12 it can be seen that at $\tau=0.2$ the cavitation region is clearly visible only at $U=40$ m/s and 45 m/s. At $\tau=0.6$ the cavitation region is visible at all speeds, however at $U=40$ m/s and 45 m/s it has already reached the trailing edge of the specimen, whereas at $U=30$ m/s and at $U=35$ m/s it has expanded less significantly. By looking at the signals recorded by the probes located at the rear, all of them exhibit a descent to the vapour pressure value. It should be noted that at $U=30$ m/s, possibly due to the incipient cavitation regime, signals from rear probes P2, P4, P7, P9, and P11 exhibit oscillatory behaviour during this descent. The start time of the descent is consistent across all speeds, while the descent itself becomes sharper as the horizontal speed increases. At $U=40$ m/s and 45 m/s, all probes, except for P15 and P17 (located on $r4$), display a rise towards the atmospheric value due, to the occurrence of ventilation, which is consistent with what shown by the underwater images. The rise starts earlier at higher speed. The probes P15 and P17, being located in the region where the longitudinal curvature is rather high, remains in the cavitation region and are not reached by the ventilation front.

To gather more insight on the cavitation and ventilation modalities, especially in the final part of the impact phase, in Figure 13, the video frames at $\tau=1$ at all speeds are shown. It is possible to see that $U=30$ m/s at $\tau=1$ the cavitation region has expanded with respect to $\tau=0.6$, see Figure 11(c), but its rear edge has not moved significantly backwards. Therefore, this case can be ascribed to the *incipient cavitation regime*, also discussed in **S3** (Iafrati and Grizzi, 2019). At $U=35$ m/s the cavitation region has reached the trailing edge and a ventilation region appears, which however remains confined around the trailing edge area, similarly to what happens in the *intermediate regime*, discussed above. Finally, at $U=40$ m/s and $U=45$ m/s $\tau=1$ the ventilation front has clearly moved back towards the leading edge, therefore in these cases a *cavitation-ventilation* regime is observed. As a final comment, it can be observed that the threshold values that delineate the various regimes in **S2** are analogous to those of **S3**.

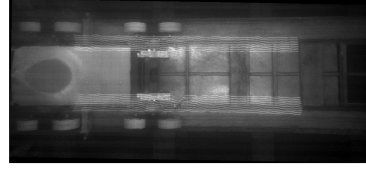
Starting from this last consideration, this aspect can be related not only to the velocity values, but also to the cavitation number, which is defined as follows:

$$Ca = \frac{p_{\text{atm}} - p_{\text{vap}}}{1/2 \rho U^2}. \quad (8)$$

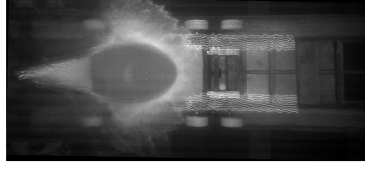
The cavitation number, other relevant nondimensional parameters, and boundary layer characteristics for the tested shape conditions **S2** and **S3** are reported in Table 3 and Table 4, respectively. Table 4 includes additional test conditions that are not analysed in detail in this article but are discussed in Iafrati and Grizzi (2019). For both shapes no cavitation occurs for $Ca \geq 0.25$. At Ca values around 0.20–0.22, incipient cavitation is observed, while for $Ca \leq 0.2$ the cavitation region extends downstream, eventually leading to ventilation. This trend with



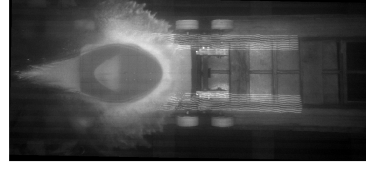
(a) $U=30$ m/s - Frame $\tau=0.2$



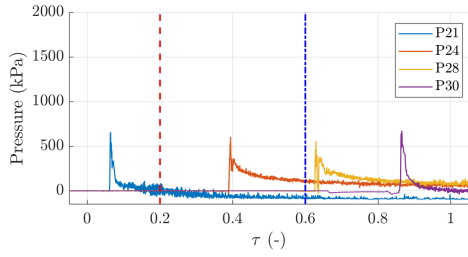
(b) $U=35$ m/s - Frame $\tau=0.2$



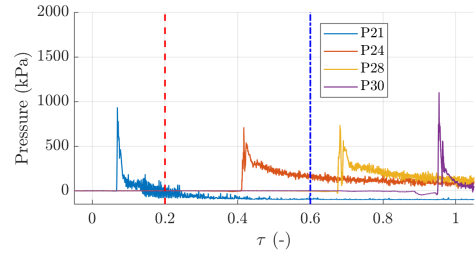
(c) $U=30$ m/s - Frame $\tau=0.6$



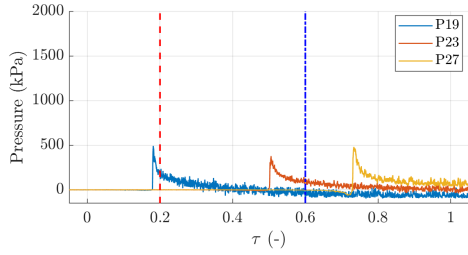
(d) $U=35$ m/s - Frame $\tau=0.6$



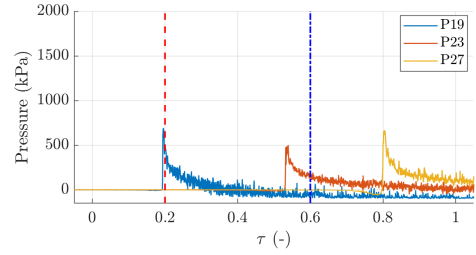
(e) p front probes - midline - $U=30$ m/s



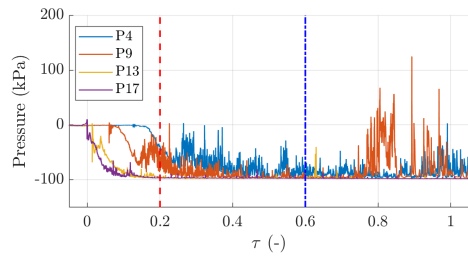
(f) p front - probes midline - $U=35$ m/s



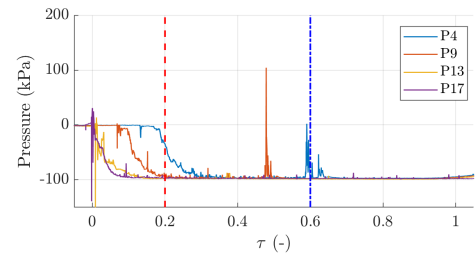
(g) p front probes - line l3 $U=30$ m/s



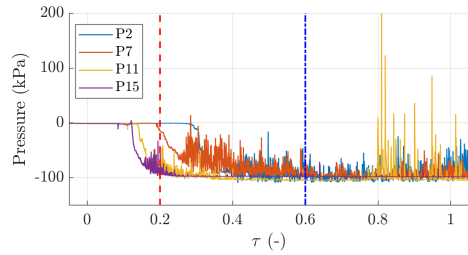
(h) p front probes - line l3 $U=35$ m/s



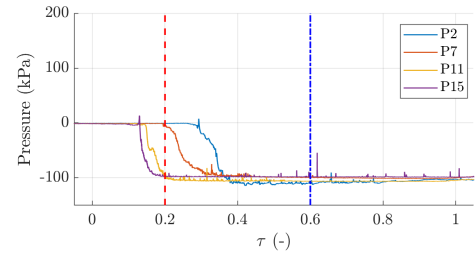
(i) p midline - rear probes - $U=30$ m/s



(j) p midline - rear probes - $U=35$ m/s

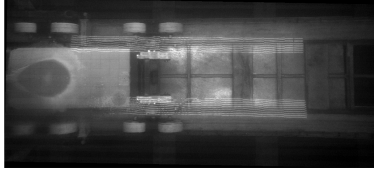


(k) p line l3 $U=30$ m/s

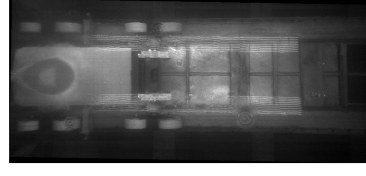


(l) p line l3 $U=35$ m/s

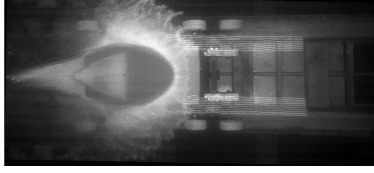
Figure 11: Front and rear pressure probe time histories and under-water video frames comparison for the tests of shape **S2**, at a pitch angle 6° and $U=30$ m/s and 35 m/s.



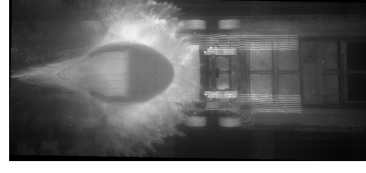
(a) $U=40$ m/s - Frame $\tau = 0.2$



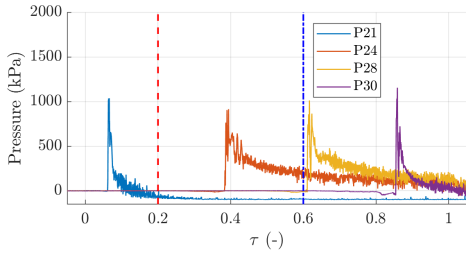
(b) $U=45$ m/s - Frame $\tau = 0.2$



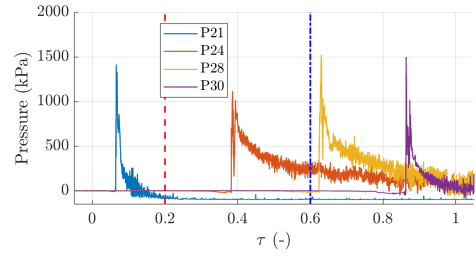
(c) $U=40$ m/s - Frame $\tau = 0.6$



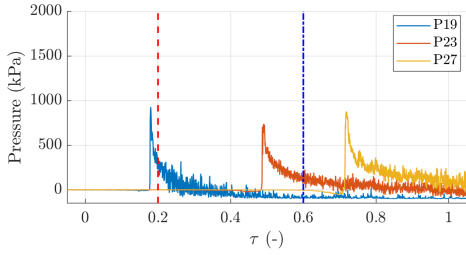
(d) $U=45$ m/s - Frame $\tau = 0.6$



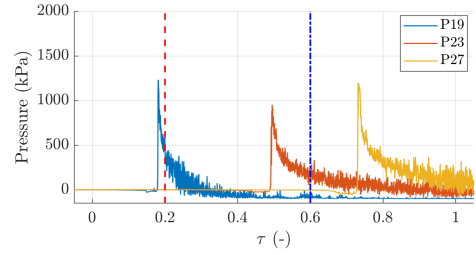
(e) p front probes - midline - $U= 40$ m/s



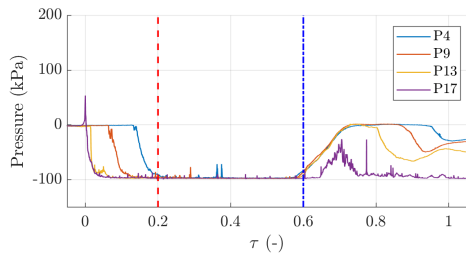
(f) p front - probes midline - $U= 45$ m/s



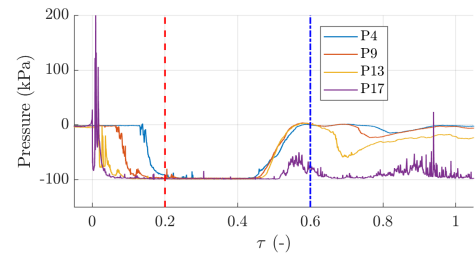
(g) p front probes - line l3 $U=40$ m/s



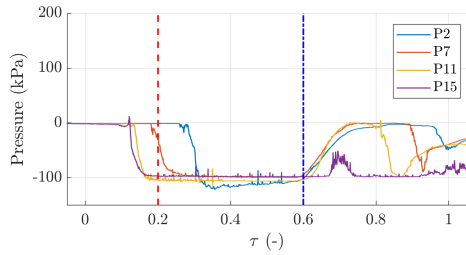
(h) p front probes - line l3 $U=45$ m/s



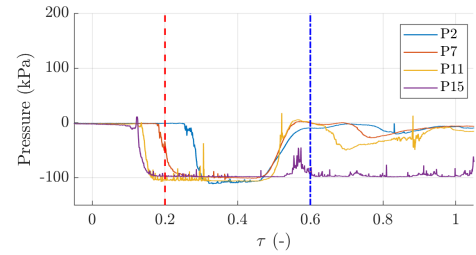
(i) p midline - rear probes - $U=40$ m/s



(j) p midline - rear probes - $U=45$ m/s

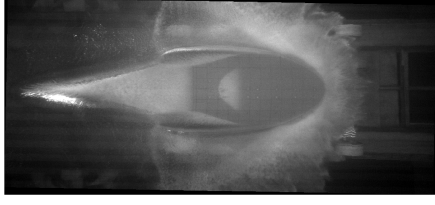


(k) p line l3 $U=40$ m/s

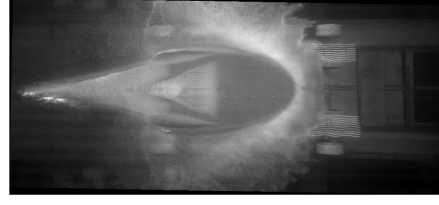


(l) p line l3 $U= 45$ m/s

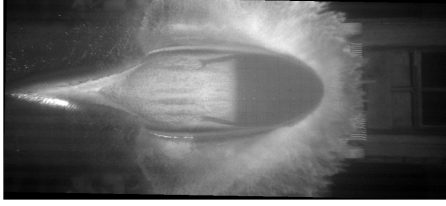
Figure 12: Front and rear pressure probe time histories and under-water video frames comparison for the tests of shape **S2**, at a pitch angle 6° and $U=40$ m/s and 45 m/s.



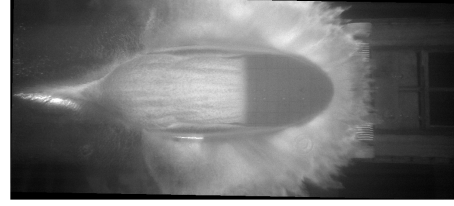
(a) $U=30$ m/s $\tau = 1$



(b) $U=35$ m/s $\tau = 1$



(c) $U=40$ m/s $\tau = 1$



(d) $U=45$ m/s $\tau = 1$

Figure 13: Frames of the underwater video taken at $\tau=1$ for the shape **S2**, at a pitch angle of $\alpha=6^\circ$ and at the different speeds.

U [m/s]	Ca [-]	Cavitation Modality	Re [-]	δ [mm]	C_f [-]	ℓ_v [m]
29.87	0.222	Incipient	3.70×10^7	14.1	0.00242	9.63×10^{-7}
34.50	0.167	Intermediate	4.28×10^7	13.7	0.00237	8.43×10^{-7}
40.25	0.122	Cavit.+Vent.	4.99×10^7	13.2	0.00231	7.31×10^{-7}
46.19	0.093	Cavit.+Vent.	5.73×10^7	12.9	0.00226	6.44×10^{-7}

Table 3: Characteristic non-dimensional and boundary layer parameters for Shape **S2**

U [m/s]	Ca [-]	Cavitation Modality	Re [-]	δ [mm]	C_f [-]	ℓ_v [m]
21.00	0.450	No Cavit.	2.60×10^7	15.1	0.00256	1.33×10^{-6}
26.80	0.276	No Cavit.	3.32×10^7	14.4	0.00246	1.06×10^{-6}
30.60	0.212	Incipient	3.79×10^7	14.0	0.00241	9.42×10^{-7}
34.50	0.167	Intermediate	4.28×10^7	13.7	0.00237	8.43×10^{-7}
35.70	0.156	Intermediate	4.43×10^7	13.6	0.00235	8.17×10^{-7}
37.20	0.143	Cavit.+Vent.	4.61×10^7	13.5	0.00234	7.86×10^{-7}
40.20	0.123	Cavit.+Vent.	4.98×10^7	13.2	0.00231	7.32×10^{-7}
45.20	0.097	Cavit.+Vent.	5.60×10^7	12.9	0.00227	6.57×10^{-7}

Table 4: CCharacteristic non-dimensional and boundary layer parameters for Shape **S3**

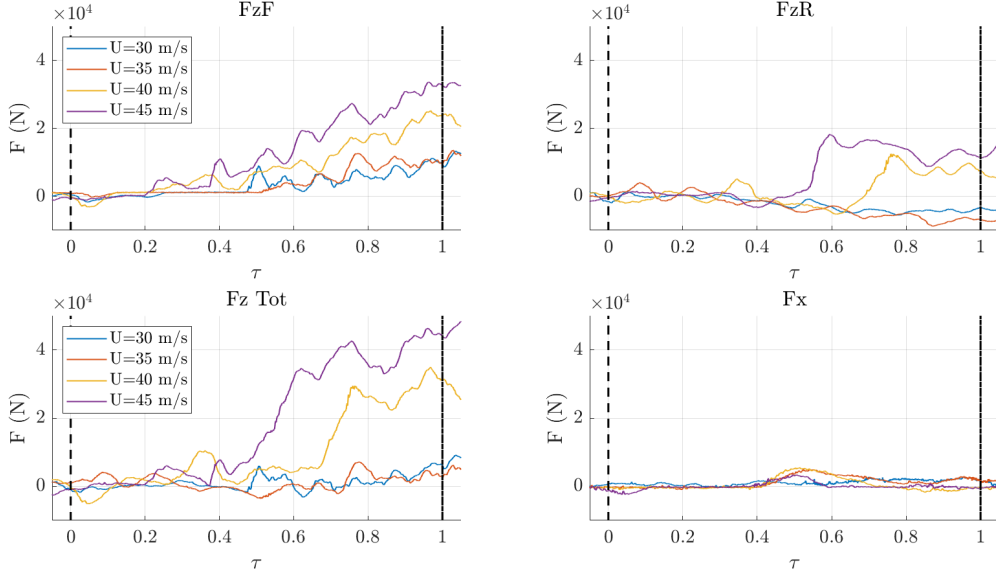


Figure 14: Time histories of the forces for the tests of shape **S2**, at pitch angle 6° and different horizontal speeds.

Ca is consistent with the observations of Wang et al. (2001) and aligns with the description of the stages of sheet cavitation on hydrofoils discussed in Huang et al. (2019).

As a final note, it should be reminded that the effect of Reynolds number in water entry flows is generally considered secondary, as supported by Moghisi and Squire (1981); Facci et al. (2015). Additionally, the pressure drop at the rear can be explained solely by potential theory (Faltinsen, 2005; Newman, 1971; Semenov and Iafrati, 2006; Riccardi and Iafrati, 2004), indicating a negligible influence of viscous effects. Furthermore, data in Tables 3 and 4 show that both boundary layer thickness and viscous length, estimated approximately using the flat plate analogy do not vary significantly across the tested range of horizontal velocities. Therefore, boundary layer effects should remain essentially consistent across the cases and speeds under investigation.

The force acting in the z -direction and measured by the load cells located at the front and at the rear are shown on the upper panels of Figure 14. The normal force recorded by the front load cells F_{zF} is more sensitive to the pressures acting on the front portion of the specimen, and for this reason it displays an increasing trend, which is consistent with the forward propagation of the spray root. The force intensity grows with speed, in line with the corresponding increase of the pressures. On the other hand, the rear load cells are more sensitive to the pressures acting on the back portion of the specimen and then, aside from the very early stage of the impact phase, they undergo the effects of the cavitation and ventilation phenomena. The load at the rear F_{zR} exhibit a similar behaviour at the different speeds, assuming more and more negative values as the cavitation area expands up to about $\tau=0.5$. Successively, when the ventilation starts, earlier for the test at $U=45$ m/s and then at 40 m/s, the force at the rear undergoes a sharp growth. It is worth noticing that this sharp variation of the loads introduces a significant displacement of the centre of loads during the water entry, which may have an important effect on the aircraft dynamics in a real ditching scenario. The total loads acting in the z - and x -directions are provided in the lower panels of Figure 14. The data indicate that the x -component is much smaller than the z -component and is characterized by a small hump occurring about $\tau=0.5$. Although already visible in terms of the rear and forward components, the total z -force is characterized by a large increase with the horizontal speed, starting from the time at which the ventilation starts. Before that time, the positive force in the front part is

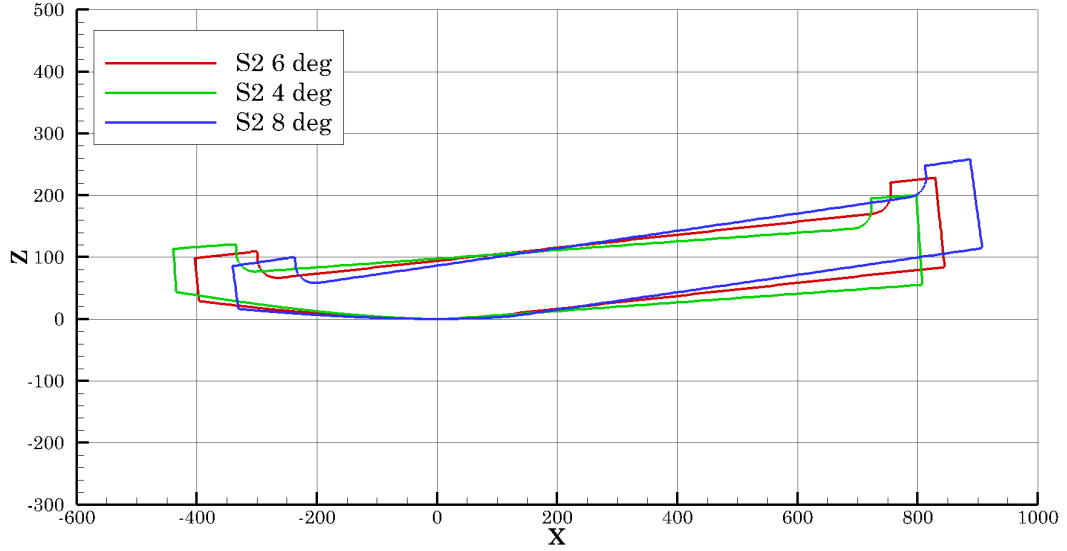


Figure 15: Comparison among the midline profiles of the shape **S2** at different pitch angles and aligned with respect to the first contact point **H**.

partly balanced by the negative loads at the rear. When ventilation starts, there is a significant increase in the total loads due to the jump in the pressure values acting on the rear portion of the specimen. A positive contribution in this time interval also derives from the increase in the front force, as a consequence of the growth of the wetted area and to the forward propagation of the spray root, with the associated pressure peak.

3.4 Effect of the pitch angle

The effect of the pitch angle on pressures and loads is somewhat more complicated by the fact that the first contact point **H** changes with it, and therefore the local geometry, in particular the longitudinal curvature around the first contact point, is different. This feature is highlighted in Figure 15, where the mid-plane sections of the specimen **S2** at the three pitch angles of 4° , 6° and 8° , aligned with respect to the first contact point, are plotted. It is worth noticing that the differences among the three profiles are not so relevant behind **H** but are very evident in the front part. As the first contact point **H** moves backwards as the pitch angle increases, the relative positions of the probes with respect to the point of initial contact are not the same, as shown in Figure 16.

In figure 17 the underwater frames at $\tau = 0.6$ and $\tau = 0.9$ for the different pitch angles are shown, together with the edges of geometric intersection between the specimen inclined at different pitch angles and the still water level at $\tau = 0.6$ and $\tau = 0.9$. By comparing the wetted area with the geometric intersection areas, a large consistency is found, aside from the presence of the cavitation and ventilation zones at the rear as well as the pile-up and the spray region in front.

The expansion of the cavitation zone to the trailing edge is observed to be faster at higher pitch angles and consequently the onset of ventilation occurs earlier. Such a situation is expected. In fact, as clearly shown in Figure 15 the slope gradient about the point **H**, while traversing the lower specimen profile from the leading edge to the trailing edge, is more pronounced in the case of higher pitch angles. This results in the development of lower pressures at the rear during the impact phase, thereby facilitating a faster expansion of the cavitation region. In addition, it is observed that at 6° and at 8° and at $\tau = 0.6$ the cavitation region has already reached the trailing edge and a ventilation front has already started propagating

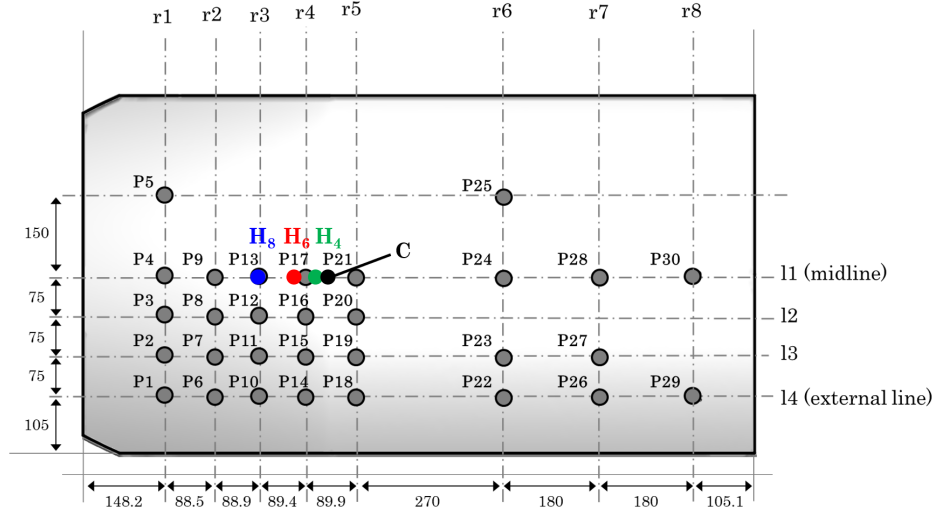
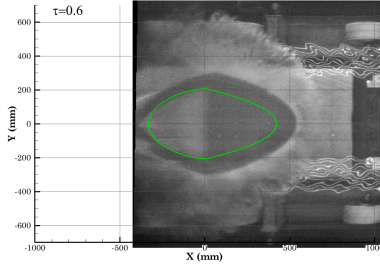
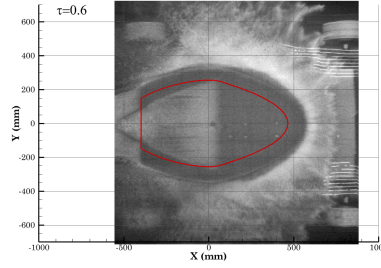


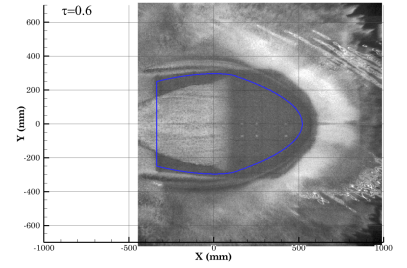
Figure 16: Position of the curvature change point **C** and of the points of first contact **H₄**, **H₆** and **H₈**, which correspond to the pitch angles of 4°, 6° and 8°, respectively.



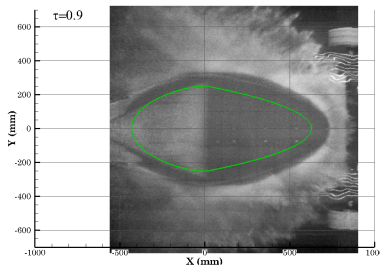
(a) Pitch 4° – $\tau=0.6$



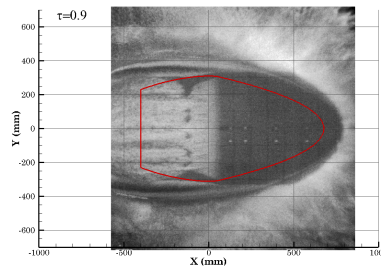
(b) Pitch 6° – $\tau=0.6$



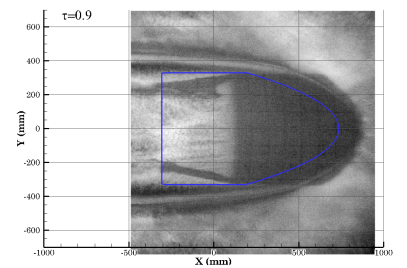
(c) Pitch 8° – $\tau=0.6$



(d) Pitch 4° – $\tau=0.9$



(e) Pitch 6° – $\tau=0.9$

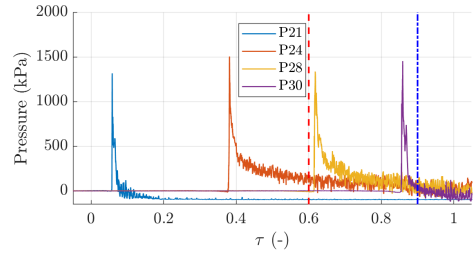
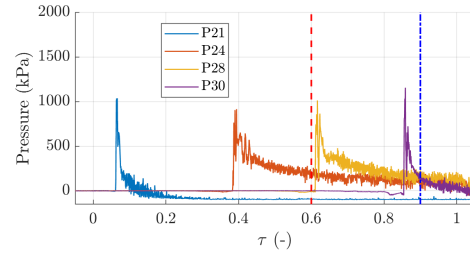
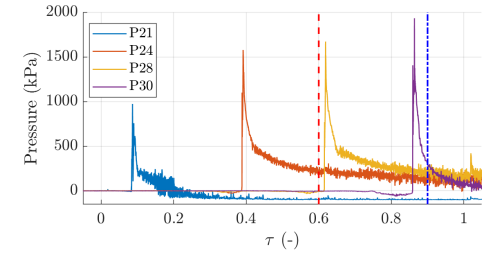
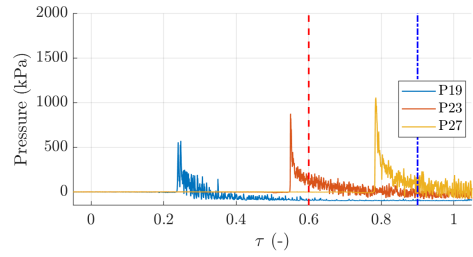
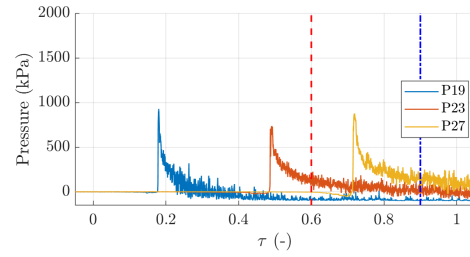
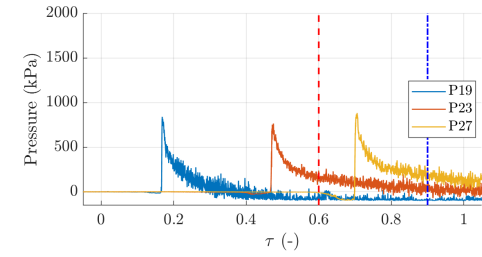
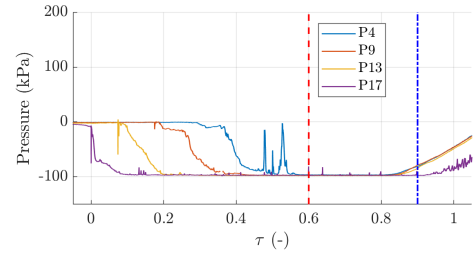
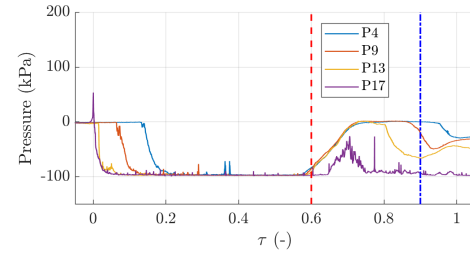
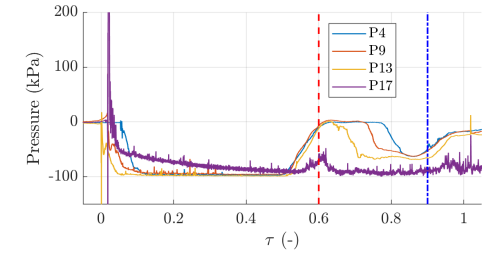
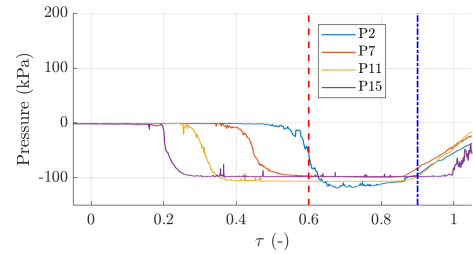
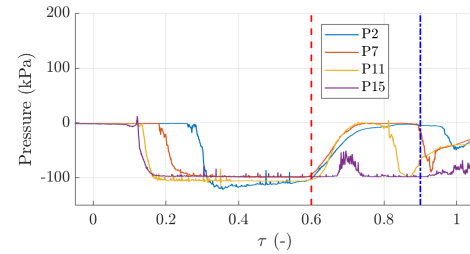
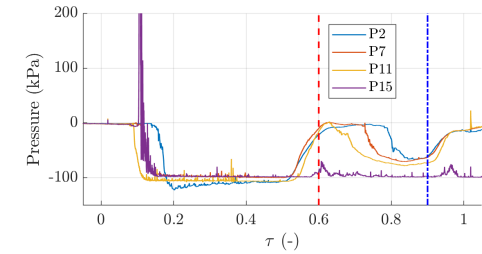


(f) Pitch 8° – $\tau=0.9$

Figure 17: Under-water frames comparison at $\tau=0.6$ and 0.9 for the specimen **S2** at $U=40$ m/s and at the pitch angles 4°, 6° and 8°.

forwards. Instead, at 4° the shape of the cavitation region has not changed relevantly between $\tau=0.6$ and $\tau=0.9$. Such a situation is similar to the case of the intermediate cavitation regimes discussed in Section 3.3.

In Figure 18(a-f) and in Figure 18(g-l) the time histories of the pressures recorded by the probes located along the midline $l1$ and line $l3$ are shown for the groups of rows from $r5$ to $r8$ and from $r1$ to $r4$, respectively.

(a) p midline - Front probes - Pitch 4°(b) p midline - Front probes - Pitch 6°(c) p midline - Front probes - Pitch 8°(d) p line $l3$ - Front probes - Pitch 4°(e) p line $l3$ - Front probes - Pitch 6°(f) p line $l3$ - Front probes - Pitch 8°(g) p midline - Rear probes - Pitch 4°(h) p midline - Rear probes - Pitch 6°(i) p midline - Rear probes - Pitch 8°(j) p line $l3$ - Rear probes - Pitch 4°(k) p line $l3$ - Rear probes - Pitch 6°(l) p line $l3$ - Rear probes - Pitch 8°Figure 18: Front and rear pressure probe time histories for the specimen **S2** at $U=40$ m/s and at the pitch angles 4°, 6° and 8°.

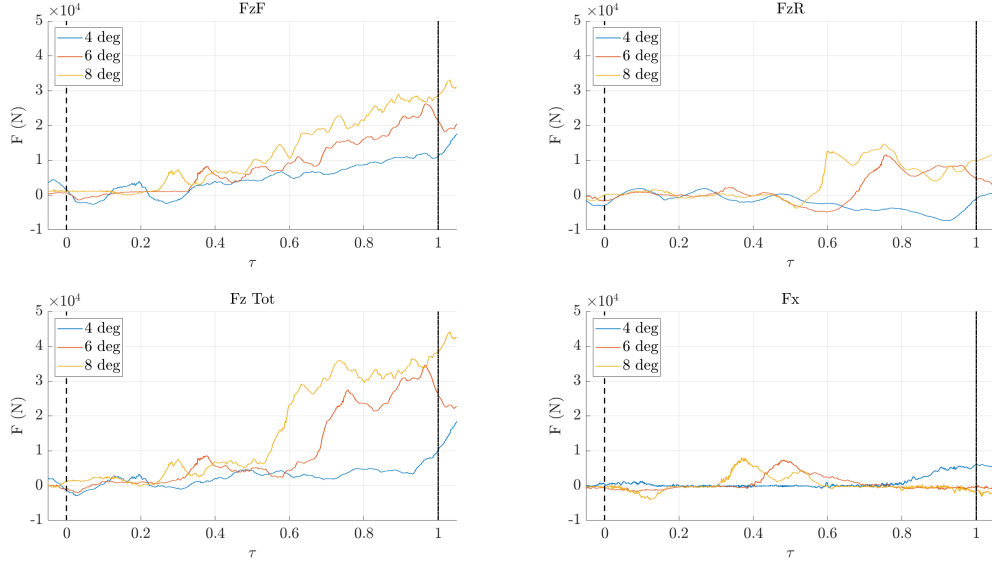


Figure 19: Time histories of the forces at the three pitch angles for the shape **S2** at $U=40$ m/s.

Looking at the pressure time histories *in the front part of the specimen* in Figure 18(a)-(f), it is observed that the pressure peaks are of the same order of magnitude for all three shapes and are delayed on the line *l3*, as a consequence of the curvature of the spray root region induced by both the body curvature and three-dimensional effects. The effect of the pitch angle is more evident by looking at the pressures values after the peak, which approach an almost constant value, higher for larger pitch angles, in agreement with what found in Iafrati (2016) for the impact of a flat plate. Something similar happens for the pressures recorded by the probes located along the sensor line *l3*.

As for the time histories recorded by the *rear pressure probes*, shown in Figure 18(g)-(l), it is shown that the drop to the vapour pressure values of all the probes located along the mid-line occurs over a shorter time period going from $\alpha = 4^\circ$ to $\alpha = 6^\circ$ and then $\alpha = 8^\circ$. Such a behaviour also is noticed at sensor line *l3*, where all pressure signals are delayed with respect to the midline due to the transverse curvature of the body. The pressure time histories also confirm that the duration of the cavitation phase is longer at 4° , where ventilation starts just at the end of the impact phase, while at both 6° and 8° it starts at about $\tau = 0.6$. It also appears that at 6° and 8° , when ventilation occurs, the pressure rise to the atmospheric pressure is quite sharp. In contrast, at 4° , the pressure growth is much milder. Such a pressure behaviour, in agreement with what discussed above regarding the video frames, is again similar to the *intermediate regimes* of cavitation, also observed for the shape **S3** in Iafrati and Grizzi (2019).

As the pitch angle increases, it is observed that the peak pressure recorded by the P17 probe also increases. At 4° no evident peak appears. An explanation for such a circumstance could be that, as shown in Figure 16, since the probe P17 is located very close to the first contact, some air cushioning effects may enter into play. Air cushioning may induce a local lowering of the free surface, especially for water entry at high speed and at low pitch angles, as discussed for flat plates in Iafrati et al. (2015). Air entrapment may also occur at higher pitch angles during the initial moments of the water impact, which may explain why a positive pressure peak is not recorded by the probe P13, which at 8° pitch is located at the first contact point.

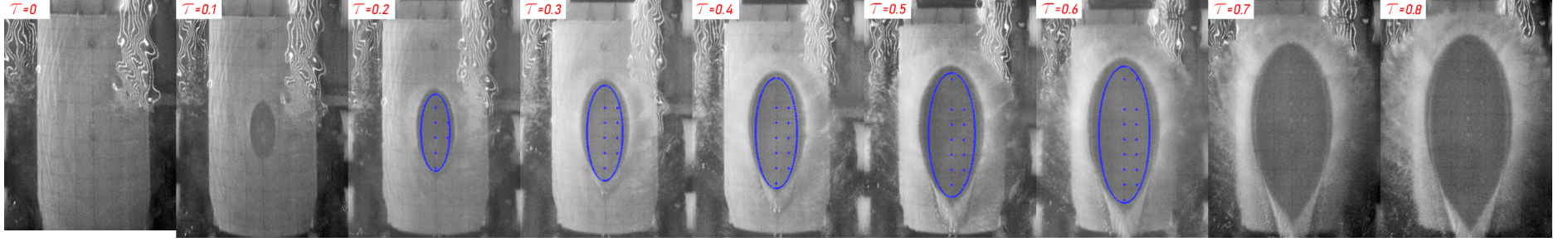
The time histories of the loads at the three pitch angles are shown in Figure 19. It can be observed that, as expected, the forces at the front increase as the pitch angle increases by about a factor 2 or more, as the pitch angle passes from 4° to 8° . The forces at the rear remain very low up to about half of the impact phase. Then, at 4° the negative loads are more evident,

whereas at 8° a sudden jump to higher values occurs as a consequence of ventilation.

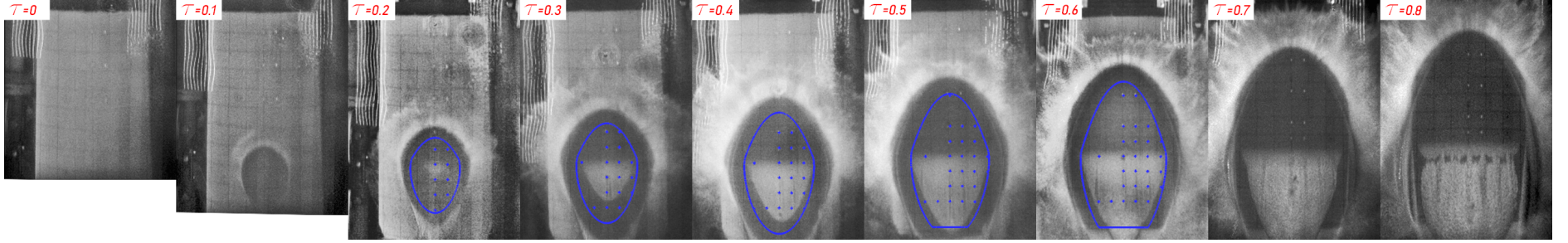
3.5 Effects of the body curvatures

Another aspect worth of investigation is the role played by the body curvatures. As already detailed in Section 2.2, three different shapes are considered. The specimens **S2** and **S3** have the same longitudinal profile in the mid-plane but different curvatures in the transverse direction, **S3** being characterized by a rather “flat” elliptical cross-section, while **S2** by a circular cross-section. The specimen **S1B** has a somewhat smoother longitudinal profile compared to the others and a circular cross section, but with a smaller radius than **S2**.

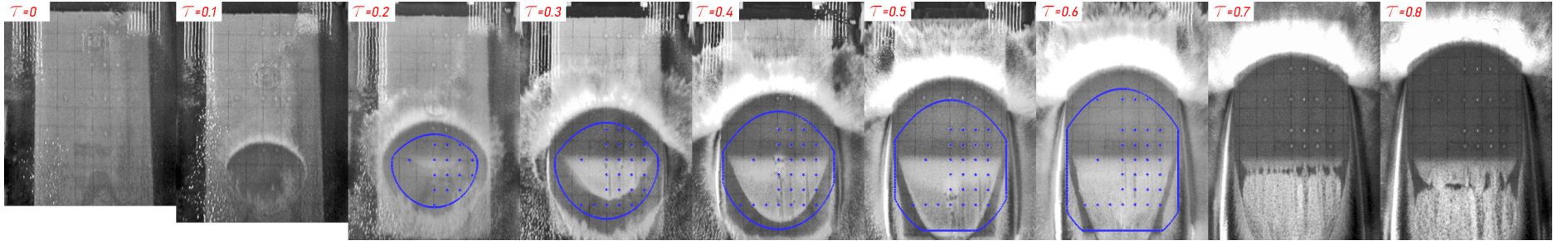
In order to gain insight on the shape on the spray in front and of the cavitation and ventilation phenomena at the rear, the underwater video-frames taken for the different shapes from $\tau=0$ to $\tau=0.8$ are shown in Figure 20. The frames are cropped and aligned with respect to the specimen leading edge, to facilitate the comparison. The edges of the geometric intersection areas with the still water level from $\tau=0.2$ to 0.6 are superimposed to the corresponding pictures.



(a) Shape **S1B**



(b) Shape **S2**



(c) Shape **S3**

Figure 20: Under-water video frames of the specimens **S1B**, **S2** and **S3** during the water entry $U=40$ m/s and pitch angle 6° from $\tau=0$ to $\tau = 0.8$. For the frames from $\tau=0.2$ to $\tau = 0.6$ the edges of the geometric intersection area with the still water level are also plotted in blue. The direction of water entry is from bottom to the top.

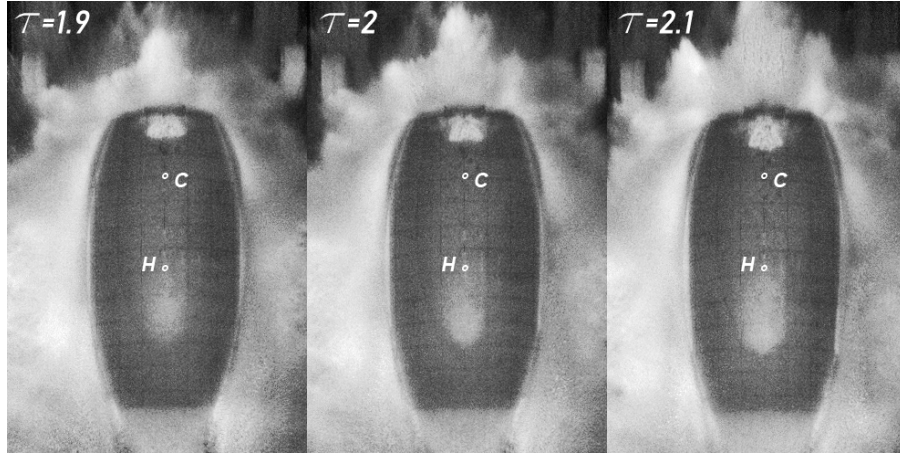


Figure 21: Cavitation area observed in the shape **S1B** after the end of the impact phase for the test at $U = 40$ m/s and pitch angle 6° . The points **H** and **C** are also superimposed. The direction of water entry is from bottom to the top.

By looking at the underwater images, it can be seen that for **S1B**, due to the smoother longitudinal curvature, the first point of contact is in the centre of the specimen. (see also Figure 4) and, differently from **S2** and **S3**, the wetted area is rather symmetric with respect to the transverse line passing through the first contact point. In the time interval from $\tau = 0.2$ to $\tau = 0.6$ it is also evident that for **S1B** the geometric intersection area exhibits analogous symmetry and is evenly smaller than the wetted area in all directions, which implies a rather uniform pile-up all around. Transversally, the width of the wetted area reflects the differences in the cross sections, therefore **S1B** has the narrowest section, due to the smaller radius of curvature, whereas **S3** has the broadest one due, to the elliptical profile.

The difference in the transverse curvatures is also responsible for the differences in the curvature of the forward propagating spray.

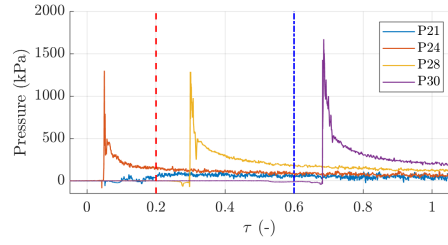
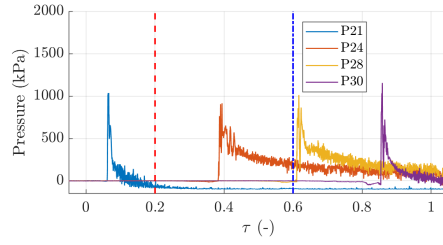
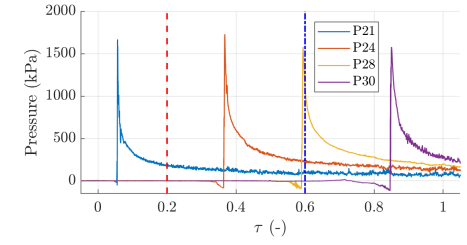
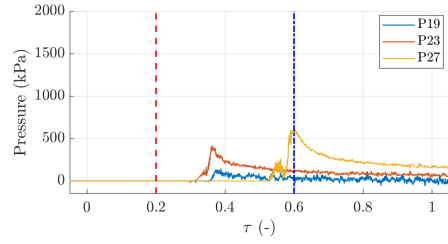
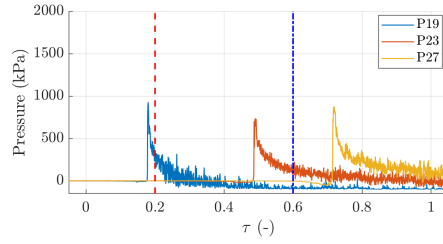
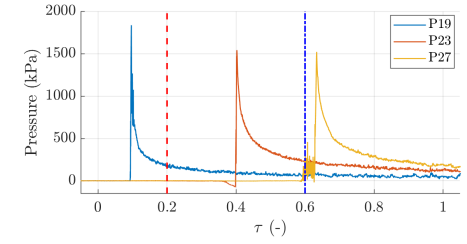
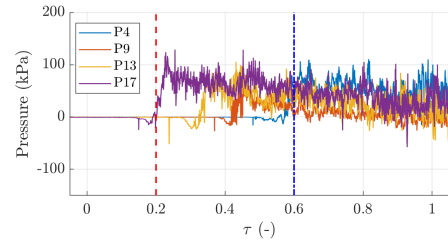
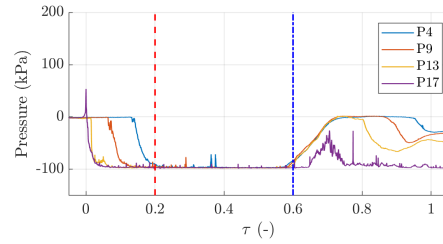
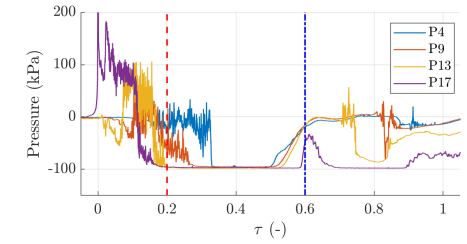
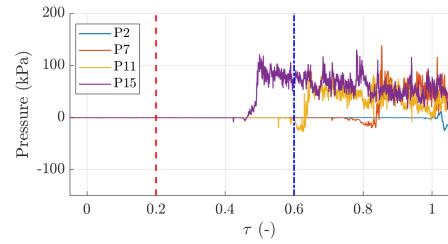
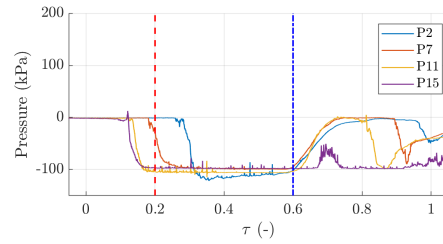
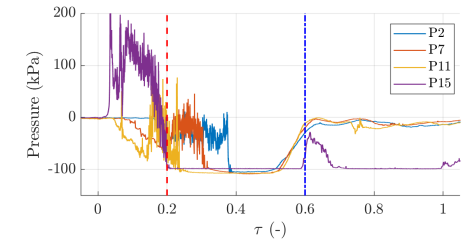
It is also evident that in **S1B** no cavitation region appears during the impact phase, unlike in **S2** and **S3**. As explained in the previous sections, in a $2D+t$ approximation, the longitudinal curvature at the rear of the body transform the water entry problem into a water exit one. As such, the smoother is the longitudinal curvature, the lower is the water exit speed and the lower is the reduction in the pressure.

As observed for the shape **S2** in Section 3.2, also for the shape **S3** the cavitation region expands in the rear part, whereas the front edge appears to be fixed at approximately the point of curvature change **C**. This is evident in the frames shown in Figure 20. As already noted in Section 3.3 the differing transverse profile between **S2** and **S3** does not alter the fact that the same regimes of evolution of the cavitation region occur, and the threshold values of U that delineate them are similar. However, in agreement with the findings of Spinoso et al. (2022) the pressures at the rear in **S3** are expected to be averagely lower (more negative), due to the lower three-dimensionality of the flow. This results in the cavitation region having a faster expansion, which also leads to an earlier formation of the ventilation zone for this shape. A more detailed analysis of the backwards expansion of the cavitation region is provided in Section 3.6, where this assertion is verified in a quantitative manner.

Although in a much less evident form, cavitation occurs also for specimen **S1B** at the same impact conditions but, as shown in Figure 21, at a much later stage starting from $\tau \simeq 1.9$. In this case, the front edge of the cavitation region appears to be situated in close proximity of the first contact point, whereas the rear edge does not exhibit a significant backward expansion in time. This situation is somewhat consistent with the incipient cavitation regime described in Section 3.3 and in Iafrati and Grizzi (2019). However, as it can be seen in Figure 21, at those

times the leading edge of the specimen is already below the still water level, and a strong jet is formed at the front, which propagates towards the trailing edge. In this phase the trolley undergoes a sharp deceleration, and therefore the flow conditions are rather uncertain. For this reason the dynamics of the cavitation region for the specimen **S1B** is not discussed further.

The above considerations are supported by the time histories of pressures along the mid-line and along line *l3*, which are shown in Figure 22. It is worth noting that in the shape **S1B**, due to the different location of the first contact point, the probes located in front portion do not include those on the row *r5* (see again Figure 16).

(a) p midline - Front probes - Shape **S1B**(b) p midline - Front probes - Shape **S2**(c) p midline - Front probes - Shape **S3**(d) p Line l3 - Front probes - Shape **S1B**(e) p Line l3 - Front probes - Shape **S2**(f) p Line l3 - Front probes - Shape **S3**(g) p midline - Rear probes - Shape **S1B**(h) p midline - Rear probes - Shape **S2**(i) p midline - Rear probes - Shape **S3**(j) p Line l3 - Rear probes - Shape **S1B**(k) p Line l3 - Rear probes - Shape **S2**(l) p Line l3 - Rear probes - Shape **S3**Figure 22: Front and rear pressure time histories for the three shapes, at $U=40$ m/s and at a pitch angle of 6° .

Looking at the mid-line probes located in the *front part* of the specimen, apart from some differences in the peak values, the pressures after the peak display a rather similar behaviour. The effect of the different curvature in the transverse direction appears evident when comparing the time delays between probes located across the same sensor row. The largest delays appears in **S1B**, whereas the the smallest one in **S3**. This circumstance can be attributed to the larger curvature of the spray root in the specimens with a higher transverse curvature, which allows for a greater possibility of the fluid to escape from the sides. For the same reason, the pressure values recorded by the probes along the line *l3* are lower for the specimens with higher transverse curvature, i.e. **S1** and **S2**.

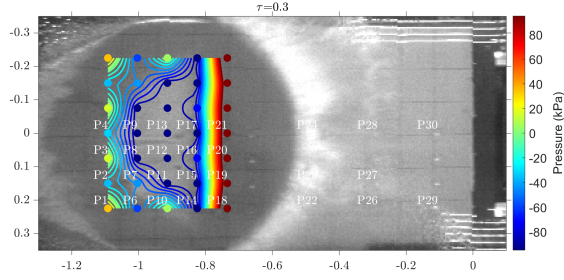
The time histories of the pressure measured by the *rear probes* for **S1B** are generally positive. Differently from what happens for **S3**, where the probes display a peak of small amplitude followed by a rapid descent and a sharp drop to the negative vapour pressure value, for **S1B** the pressures display a sharp rise to a maximum value and then a very gentle decay, with some probes assuming negative values at about the end of the impact phase.

Comparing the **S2** and the **S3** pressure time histories at the rear, it can be seen that, presumably due to the lower transverse curvature and the lower local deadrise angle, evident pressure peaks appear only in **S3**. In the next stage, for both **S2** and **S3** the pressures at the rear exhibit sharp drops to the vapour pressure value, which is consistent with what shown by the underwater images. The delay between the pressure drops recorded by the probes placed on the same row between lines *l1* and *l3* (for example between P17 and P15 or between P13 and P11) is greater in the case of S2, compared to S3. This is a consequence of the larger curvature of the rear edge of the cavitation region, which appears as a D-shape more elongated in the longitudinal direction (see Figure 20(b) and (c)). The ventilation phase starts earlier in **S3** than in **S2**, which confirms that the expansion of the cavitation region is faster for the former shape, as the cavity reaches the trailing edge earlier in time.

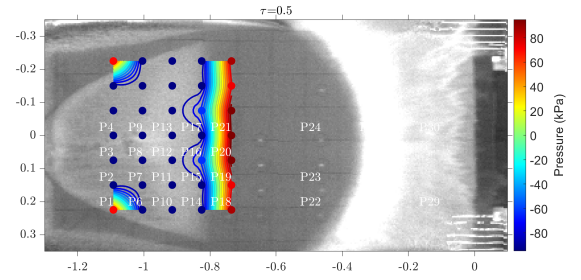
The difference between the the pressure fields of **S2** and **S3** on the bottom can also be visualized when comparing pressure iso-lines which in Figure 23, are superimposed on the corresponding video frames at $\tau = 0.3$ and $\tau = 0.8$ and from $\tau = 0.5$ to $\tau = 0.6$ with a finer non-dimensional time resolution of $\Delta\tau = 0.02$. Firstly, it can be observed that, due to the “flatter transverse profile” the pressure at the front edge of the cavitation region rises more sharply and uniformly in the transverse direction for the shape **S3**, compared to **S2**. At $\tau=0.3$ the shape of the cavitation area in **S3** is still in agreement with the pressure iso-lines, but it has a less elongated shape compared to **S2**. However, as the cavitation region expands faster in **S3**, at $\tau=0.6$ the rear edge has already reached the trailing edge and the ventilation front has already moved forwards, up to the point *C*. At $\tau=0.8$, the development of the ventilation zone has further evolved.

Ventilation in **S3** occurs in between $\tau=0.5$ and $\tau=0.6$. In Figure 23 the evolution of the process is visualised at six time instants within this non-dimensional time interval. The mechanism of formation and development of the ventilation front in **S3** is similar to **S2**, with a curved front starting from the centre at the trailing edge, which evolves very shortly into a straight one and reaches the point *C*.

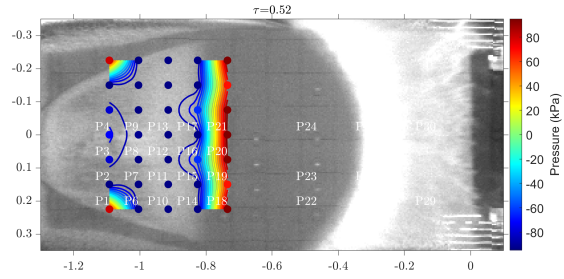
The comparison in terms of the *z*-force time histories for the three shapes is shown in Figure 24. The data indicates that the load measured at the front is characterised by an increasing trend for all three shapes. The growth rate is higher, as the transverse curvature decreases, which is consistent with the pressure behaviour discussed above. The load at the rear exhibit a slightly decreasing trend for **S1B**, whereas for both **S2** and **S3** an initial decreasing trend is observed, associated with the onset of cavitation, followed by a rather sharp rise, related to the ventilation phase. As ventilation starts earlier for shape **S3**, the sharp rise occurs earlier, consistently with the pressure time histories. No substantial differences are found for the *x*-component of the force for the three specimens, which is always very small compared to the



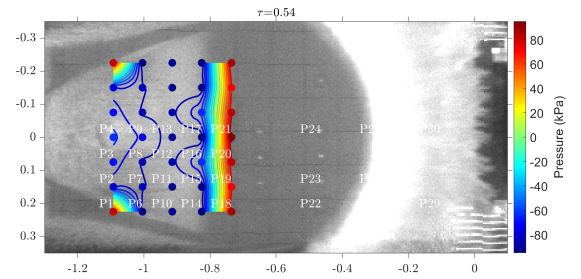
(a) $\tau = 0.3$



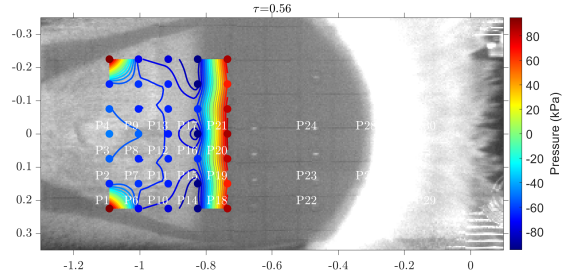
(b) $\tau = 0.50$



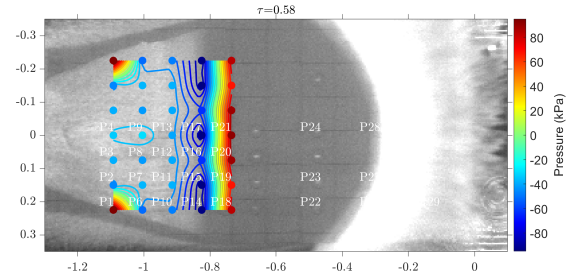
(c) $\tau = 0.52$



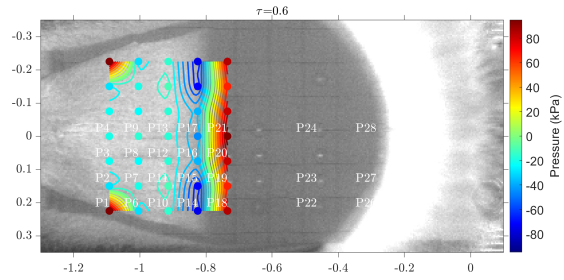
(d) $\tau = 0.54$



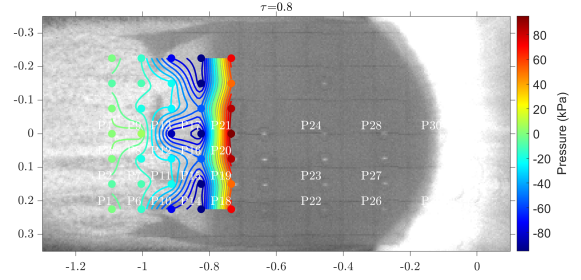
(e) $\tau = 0.56$



(f) $\tau = 0.58$



(g) $\tau = 0.6$



(h) $\tau = 0.8$

Figure 23: Pressure iso-lines in the rear part of the specimens **S3** overlapped to the underwater video frames for the water entry at $U=40$ m/s, at $\alpha = 6^\circ$ at the specified τ values. The symmetry about the mid-line is exploited.

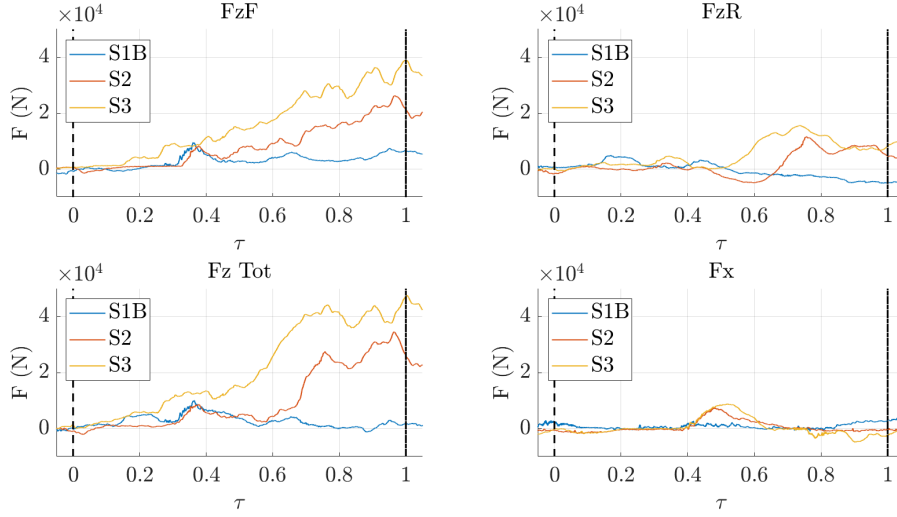


Figure 24: Time histories of the forces for the three shapes at $U=40$ m/s and pitch angle 6° .

z -component.

3.6 Cavitation zone propagation velocity

The underwater videos and pressure data can be exploited to derive more precise information on the dynamics of the cavitation region, not only from the qualitative point of view, but also from the quantitative point of view. The occurrence of cavitation exerts significant effects in terms of both load amplitude and moments, and thus the centre of loads. It is therefore of great importance to analyse its evolution in more detail, and to evaluate, on a quantitative basis, the influence of the body curvatures upon it, especially the transverse curvature.

For this purpose a *propagation velocity of the cavitation region*, denoted as U_{cav} , is introduced, which is the velocity at which the rear edge of the cavitation zone moves backwards in the trolley reference frame. This propagation velocity can be retrieved either from the analysis of the underwater video frames or from the pressure signals, as follows. Starting from the *underwater images* the edge of the cavitation region is identified and the furthest point at the back is marked for all frames, which are separated by a constant time interval. The position of the rear edge in the pictures can be determined within ± 2 pixels, which makes the calculation of the propagation velocity rather accurate. The propagation velocity is computed as an average velocity from the instant in which the cavitation region clearly appears in the frames up to the instant at which it reaches its maximum extension, i.e. when the region reaches a steady size in the *incipient cavitation regime* or as soon as the region reaches the trailing edge in the *cavitation-ventilation regime*. The propagation velocity of the cavitation region can also be determined from the *time histories of the pressure* measured by the different probes. In fact, the passage of the cavitation front corresponds to the sharp drop to the vapour pressure value. Hence, being the position of the probes on the specimen known, the velocity can be determined from the time delay between the pressure drops recorded by different probes. Since the raw pressure signals, as observed above, are often very noisy and display significant spikes, to facilitate the estimation of the time delays, a de-noising procedure has been developed in MATLAB[®], which includes in sequence a Continuous Wavelet Transform - based filter, a conventional low-pass filter and a moving average. Hence, the time delay is calculated through a cross-correlation of the denoised signals, with the objective of identifying the time shift that optimises the degree of overlap between the drop portions. The process is illustrated in detail in Figure 25. The estimated propagation velocities of the cavitation region U_{cav} , based on the

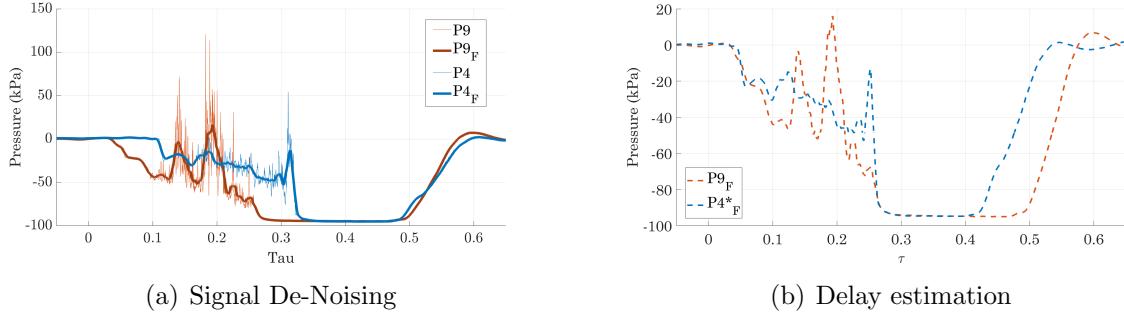


Figure 25: Comparison of (a) two sample signals recorded by the pressure probes P4 and P9 before and after the de-noising procedure and (b) overlapping of the signal P9 and the signal P4*, which is the one recorded by P4 and translated in time for the delay estimation.

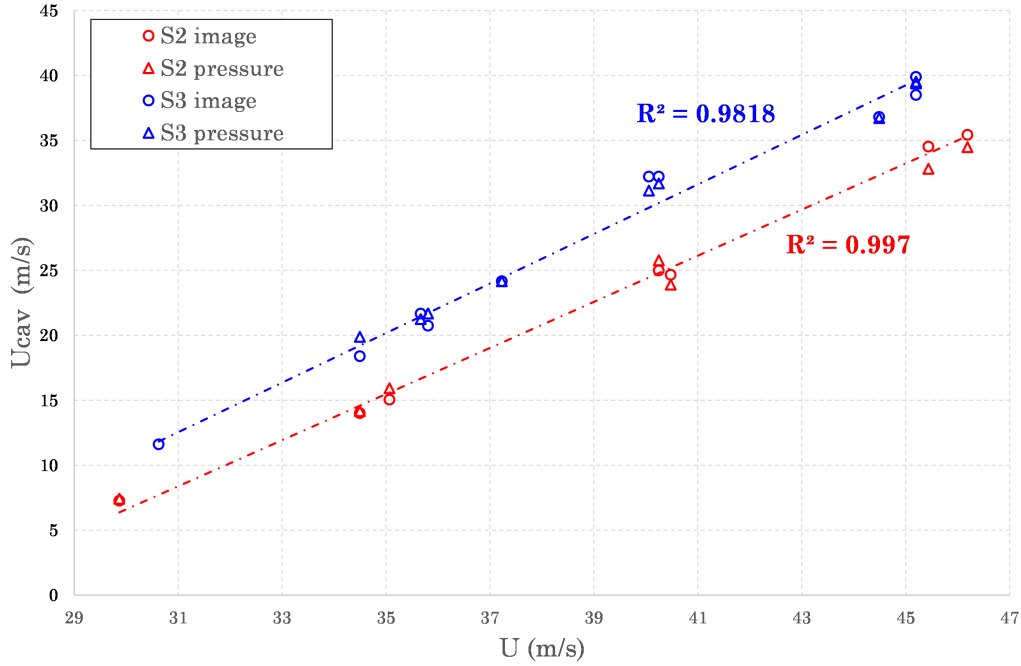


Figure 26: Propagation velocities of the cavitation area for the three shapes and as a function of U , using the method bases on image analysis (circles) and on pressure data (triangles). Linear trend lines are added using the results of the image analysis method.

image analysis and on the pressure time histories, are plotted in Figure 26 for the shapes **S2** and **S3** at 6° , velocity ratio $V/U=0.0375$, and different horizontal speeds. It is worth noticing that in the graph supplementary test conditions with different horizontal velocities are considered, in addition to those listed in Table 2. U_{cav} is plotted as a function of the horizontal velocity U , and linear fits of the data derived from the image analysis are also plotted, which both have a coefficient of determination R^2 very close to 1. It is worth noticing that the propagation velocity computed by using the pressure signals are very much in line with those derived from the image analysis. The above results indicate that U_{cav} is directly proportional to the horizontal speed U and that the coefficient of proportionality is between 1.77 and 1.91 for the shapes **S2** and **S3**, respectively. There is a vertical offset between the two trends, with U_{cav} being higher for **S3** compared to **S2**, as a consequence of the lower transverse curvature that reduces the three-dimensional effects on the resulting flow, consistently with the considerations presented in Section 3.5.

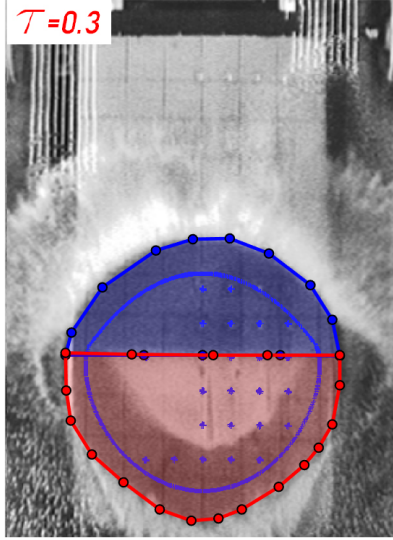
3.7 Wetted area evolution

In the pioneering works of Von Karman (1929) and Wagner (1932) on vertical water entry, the growth of the wetted area is related to the time variation of the added mass and, therefore, to the impact loads. The primary distinction between the two theories is that, whereas von Karman's theory considers solely the geometric intersection of the body with the free, the Wagner method also accounts for the water pile-up at the spray. In the work of Iafrati (2016) on the water entry of flat plates with a high horizontal speed, it was observed that the value of the pressure peak and the propagation of the spray root during the impact phase are related. Consequently, the evolution of the wetted area and the loads are also subject to a similar relationship. In light of the aforementioned discussion, it can be reasonably assumed that a comparable analogy can be expected in the front part of double-curvature specimens, where the pressures are found to be positive in all areas. Conversely, at the rear, the occurrence of negative pressures and, consequently, of cavitation and ventilation renders such an analogy invalid. Given the aforementioned considerations, it is considered useful to conduct a more detailed investigation into the evolution of the wetted area in relation to the geometric intersection area.

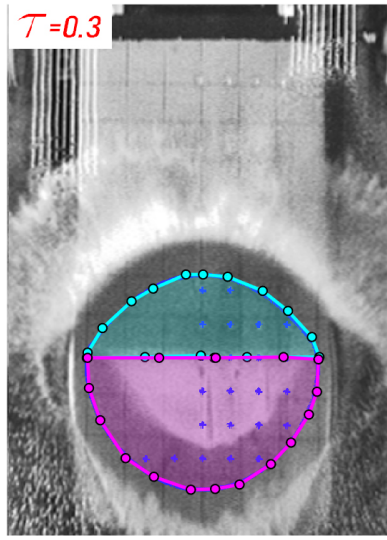
Looking again at Figure 20, referring to the water entry of the three shapes at $U=40$ m/s, $\alpha=6^\circ$ and $V/U=0.0375$, as mentioned already in Section 3.2, the wetted areas are identifiable as the darker regions at the centre of the specimen. Inside the wetted area the brighter zone, when present, is the cavitation region. It is observed that, due to the pile-up effect, for **S1B** and **S2** the actual wetted area is broader than the geometric intersection area with the undisturbed free surface at τ in between 0.2 and $\tau=0.6$. This is also the case for the shape **S3** up to $\tau=0.3$. However, for **S3** from a value of τ between 0.4 and 0.5, if the pile-up effect persists at the front, at the rear of the specimen, in addition to the cavitation/ventilation zone at the middle, some bright zones emerge at the sides. These zones are most likely caused by ventilation originating from the sides of the specimen and developing as a result of the low pressures in the middle. Two dark narrow regions of wetted area are still present between the cavitation/ventilation zones in the middle and the ventilation zones at the sides. In particular, it is observed that for **S3** the wetted area becomes smaller than the geometrical intersection area at a non-dimensional time τ between 0.4 and 0.5. Such an effect becomes more evident at $\tau=0.6$. A similar effect was also observed in Spinosa et al. (2022), in which a shrinking of the wetted area with respect to the geometric intersection area is observed in the planing motion of the whole fuselages **S2** and **S3**, with the effect more enhanced for **S3**, as a consequence of the lower pressures at the rear.

From the quantitative point of view it is possible to estimate the wetted area from the underwater video frames and to compare it with the geometrical intersection area. This is performed for the three shapes, using an image processing routine developed in MATLAB[®]. As shown in Figure 27, which refers to shape **S3** at $\tau=0.2$ and 0.6, three Region Of Interests (ROIs) are manually selected and their areas are computed, first as pixel counts and then as the physical area in m^2 , by multiplying the pixel count for the pixel area derived from an image calibration. In particular, the defined ROIs are the front and rear wetted surface, which are delimited by the x -coordinate of the pressure probe row $r4$, the front and rear part of the geometric intersection area, still separated by the row $r4$, and finally the cavitation area. It is worth noticing that using this routine, the wetted areas are not exactly estimated rather their projection on the plane $X - Y$, parallel to the ground.

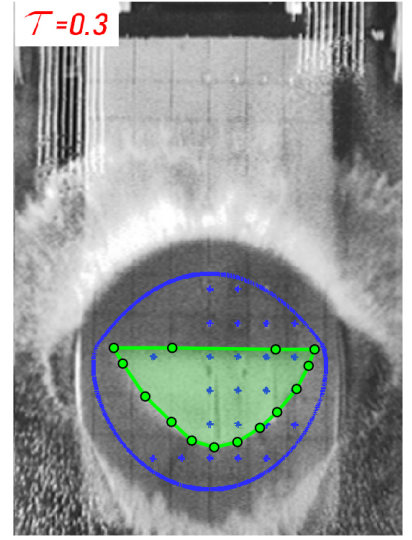
A comparison between the values of front/rear wetted areas and of the geometrical intersection from $\tau=0.2$ to 0.6 (see also Figure 20) is shown in Figure 28 for the three shapes. The values of the cavitation areas are plotted in Figure 28(g) and (h) for the shapes **S2** and **S3** respectively.



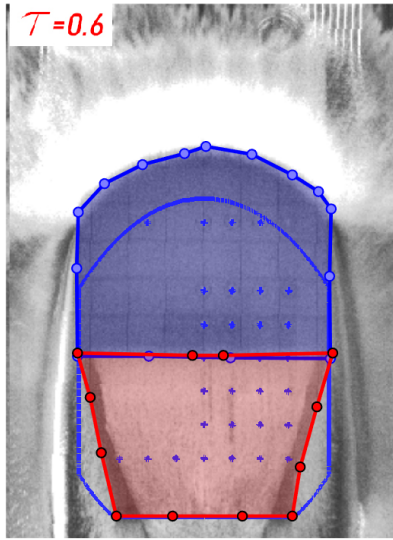
(a) Wetted Area Front/Rear $\tau=0.3$



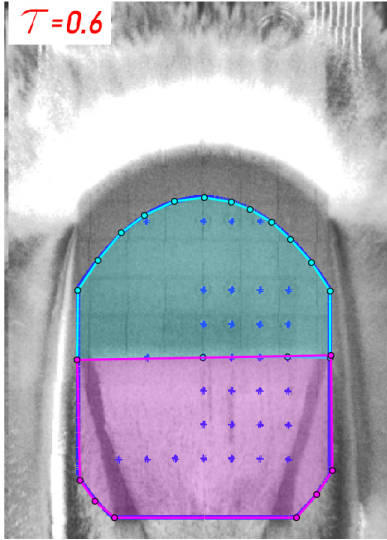
(b) Geometric Intersection Front/Rear $\tau=0.3$



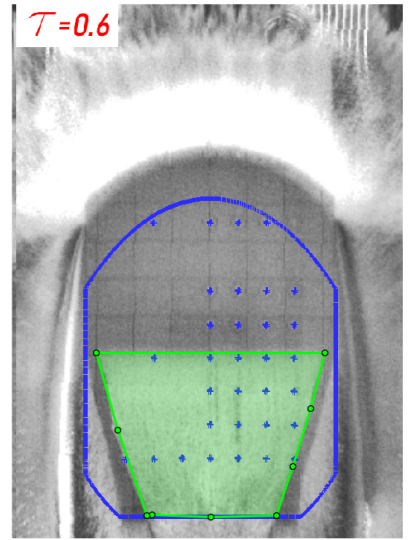
(c) Cavitation Area $\tau=0.3$



(d) Wetted Area Front/Rear $\tau=0.6$

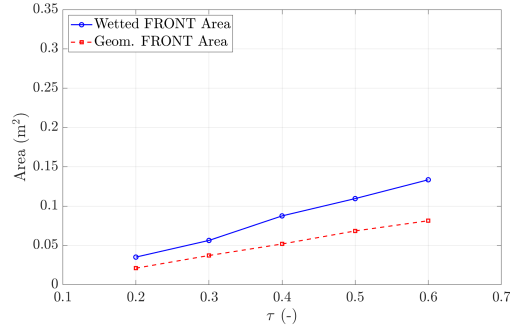


(e) Geometric Intersection Front/Rear $\tau=0.6$

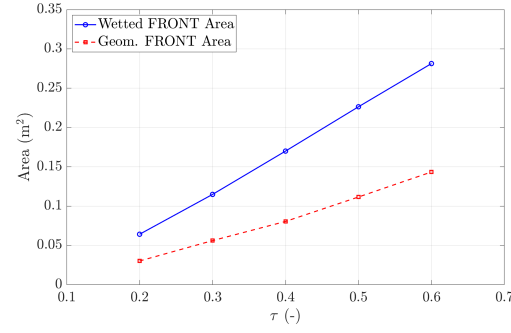


(f) Cavitation Area $\tau=0.6$

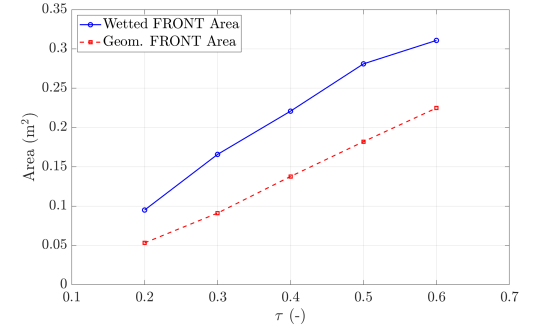
Figure 27: Definition of the ROI for (a,d) the wetted areas in front and at the rear of the specimen; (b,e) geometrical intersection area at the front and at the rear; (c,f) cavitation area for the shape **S3** at $U=40$ m/s, pitch angle 6° at $\tau=0.3$ (top) and 0.6 (bottom).



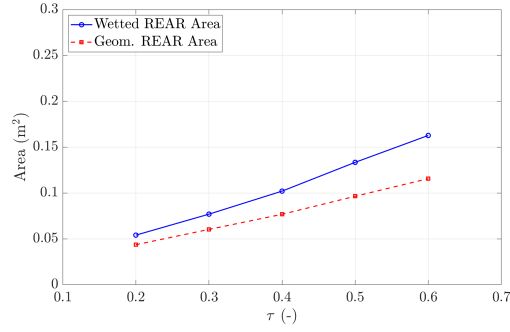
(a) Front part **S1B**



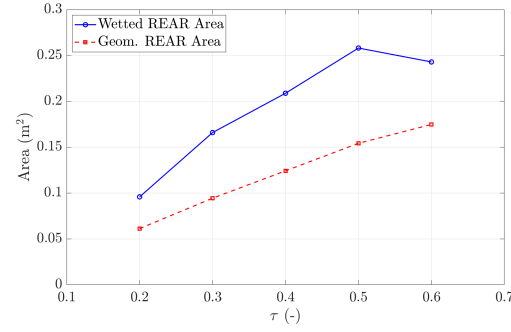
(b) Front part **S2**



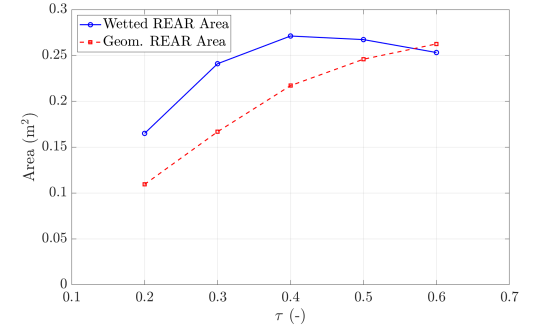
(c) Front part **S3**



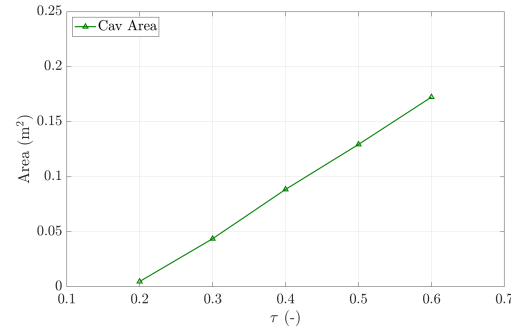
(d) Rear part **S1B**



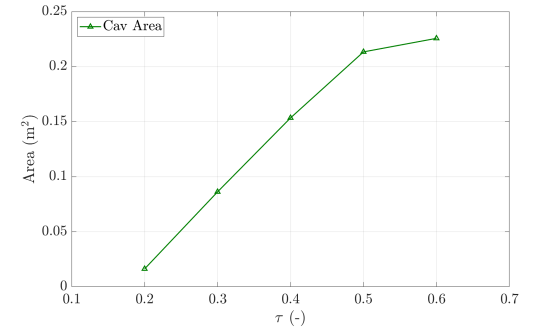
(e) Rear part **S2**



(f) Rear part **S3**



(g) Cavitation area **S2**



(h) Cavitation area **S3**

Figure 28: Variation in time wetted areas compared with the geometrical intersection area for the specimen **S1B**(a,d), **S2** (b,e) and **S3**(c,f) at pitch angle 6° at $U=40$ m/s from $\tau=0.2$ to 0.6 . In (g,h) the cavitation area as a function of τ is shown for the shapes **S2** and **S3**.

It is observed that at the front both the wetted and the geometric intersection areas grow between $\tau = 0.2$ and $\tau = 0.6$, in particular the wetted area grows at a slightly higher rate. Owing to the much smoother curvature, specimen **S1B** is characterized by the lowest growth rates. As to **S2** and **S3**, it can be noticed that in the interval $\tau \in (0.2 \ 0.6)$ the growth of the wetted area is about the same, despite the fact that **S3** exhibits a higher growth rate of the geometric intersection area.

At the rear, in the case of specimen **S1B** both the geometric intersection and the wetted areas grow in time, the latter at a slightly higher rate. In the case of **S2** and **S3**, the values of the geometric intersection area display a monotonic trend, although in the case of **S3** the growth rate exhibits a reduction after $\tau = 0.4$. The wetted area grows up to $\tau = 0.5$ and $\tau = 0.4$ for **S2** and **S3**, respectively. For **S2** the wetted surface remains almost constant afterwards, as it reaches the edges of the specimen. In the case of **S3** the occurrence of ventilation at the sides causes a shrinking of the wetted area, which progressively approaches the value of the cavitation area. For both **S2** and **S3** the cavitation area grows almost linearly in time, although for **S3** it approaches an almost constant value after $\tau = 0.5$, once the cavitation zone has reached the trailing edge of the specimen, and the rear ventilation starts.

4 Conclusions and Future Work

In this paper the water entry at high horizontal speed of rigid specimens with double curvature has been investigated, based on experimental data. The effects of the horizontal speed and of the pitch angle are analysed, keeping constant the vertical-to-horizontal velocity ratio. Three different shapes with different transverse and longitudinal curvatures have been considered.

It has been observed that the presence of a longitudinal curvature plays a key role, marking an important distinction with respect to the water entry of flat plates at similar test conditions (Iafrati, 2016). Indeed, the longitudinal curvature, depending on velocity ratio and on the pitch angles, can lead to the occurrence of negative pressures (relative to atmospheric pressure) at the rear, which can reach the vapour pressure value. This, in turn, can result in the formation of a cavitation region. Furthermore, as the region of low pressure at the rear may expands significantly during the water entry, it can favour air entrainment either from the trailing edge or from the sides, leading to ventilation. It has been shown that the transverse curvature does not influence much the cavitation modalities, however it has an effect on the loads and on the dynamics of the cavitation region, due to the increased possibility for the fluid to escape from the side, in case of higher curvature.

The pitch angle is found to affect the pressures and the loads in the front part of the body, the loads being higher for higher pitch angles, consistently with what found for the impact of a flat plate in Iafrati (2016). In addition, given the change in the gradient slope in the rear part, the modalities of cavitation may change. At the higher pitch angle a cavitation-ventilation regime is observed, whereas at the lower pitch angles the ventilation region remains confined close to the trailing edge during the impact phase.

Based on the underwater video frames and on the pressure measurements, more detailed information on the dynamics of the cavitation region and of the wetted area can be retrieved. It is observed that the propagation velocity of the cavitation region increases linearly with the horizontal speed both for **S2** and **S3**. Although the slope is approximately equivalent in both case, an offset exists between the two trends, being the propagation speed higher for **S3**, as a consequence of the lower transverse curvature.

Starting from the underwater images, quantitative estimates of the wetted area, of the the geometric intersection area with the still water level and of the cavitation area can be retrieved. A distinction is made between what happens ahead and behind the point of curvature change. The data indicate that for the shape **S1B**, the growth rate of all areas is lower, and

so is the difference between the wetted area and the geometric intersection area, compared to the specimens characterised by higher longitudinal curvatures. For shape **S3** a ventilation phenomenon from the sides has been also observed, occurring at the rear, as a consequence of the low pressures developing beneath. The occurrence of such ventilation zones causes a shrinking of the wetted area at the rear, which becomes smaller than the corresponding geometric intersection area.

In addition to contributing to a deeper understanding of the physical phenomena occurring during the water entry at high horizontal speed and of the effects induced by changes in the body shape, the present paper provides a rather wide and detailed dataset, which could be used for an accurate validation of numerical approaches for the simulation of aircraft ditching or other water entry problems. Future work will focus on developing routine-based pattern recognition algorithms to automate the selection and tracking in time of the wetted area, cavitation areas and the following ventilation front in underwater videos, which can be improved by also exploiting the information coming from the pressure probes.

Supplementary Material

Supplementary materials are available for download at: <https://www.sciencedirect.com/science/article/pii/S0029801825018931#ecom0001>

The graphical abstract can be viewed at this link: https://ars.els-cdn.com/content/image/1-s2.0-S0029801825018931-ga1_lrg.jpg

Acknowledgements

The authors also wish to thank: Flavio Olivieri, the technical supervisor of the *High Speed Ditching Facility*, who is also responsible for its maintenance. He also participated in the the execution of all the experiments; Fabio Carta, the project manager who dealt with the design of the specimens and with the installation of the instrumentation on board of them and on the facility; Mauro Sale who provided technical support during the execution of the experiments; Alessandro Del Buono who gave valuable support in the interpretation of the results.

Funding

This project has been funded from the European Union's Horizon 2020 Research and Innovation Programme under Grant Agreement No. 724139 (H2020-SARAH: increased SAFety & Robust certification for ditching of Aircrafts & Helicopters).

Declaration of interests

The authors report no conflict of interest.

References

- Abrate, S. (2011), 'Hull slamming', *Applied Mechanics Reviews* **64**(6), 060803.
- Acosta, A. (1973), 'Hydrofoils and hydrofoil craft', *Annual Review of Fluid Mechanics* **5**(1), 161–184.

- Anghileri, M., Castelletti, L., Francesconi, E., Milanese, A. and Pittofrati, M. (2011), ‘Rigid body water impact—experimental tests and numerical simulations using the sph method’, *International Journal of Impact Engineering* **38**(4), 141–151.
- Anghileri, M., Castelletti, L., Francesconi, E., Milanese, A. and Pittofrati, M. (2014), ‘Survey of numerical approaches to analyse the behavior of a composite skin panel during a water impact’, *International Journal of Impact Engineering* **63**, 43–51.
- Battistin, D. and Iafrati, A. (2003), ‘Hydrodynamic loads during water entry of two-dimensional and axisymmetric bodies’, *Journal of fluids and structures* **17**(5), 643–664.
- Bensch, L., Shigunov, V. and Söding, H. (2003), Computational method to simulate planned ditching of a transport airplane, in ‘Computational Fluid and Solid Mechanics 2003’, Elsevier, pp. 1251–1254.
- Bisagni, C. and Pigazzini, M. (2018), ‘Modelling strategies for numerical simulation of aircraft ditching’, *International Journal of Crashworthiness* **23**(4), 377–394.
- Brennen, C. E. (2014), *Cavitation and bubble dynamics*, Cambridge university press.
- Cheng, H., Chao, F. and Cheng, J. (2011), ‘Simulation of fluid-solid interaction on water ditching of an airplane by ale method’, *Journal of Hydrodynamics, Ser. B* **23**(5), 637–642.
- Climent, H., Benitez, L., Rosich, F., Rueda, F. and Pentecote, N. (2006), Aircraft ditching numerical simulation, in ‘25th International congress of the aeronautical sciences’, Hamburg, Germany, pp. 1–16.
- Del Buono, A., Bernardini, G., Tassin, A. and Iafrati, A. (2021), ‘Water entry and exit of 2d and axisymmetric bodies’, *Journal of Fluids and Structures* **103**, 103269.
- Del Buono, A. and Iafrati, A. (2025), ‘Potential-flow multisection approach for the vertical water entry of elongated bodies’, *Available at SSRN 5210872* .
- Desjardins, S. P., Zimmerman, R. E., Bolukbasi, A. O. and Merritt, N. A. (1989), Aircraft crash survival design guide. volume 4. aircraft seats, restraints, litters, and cockpit/cabin delethalization, Technical Report ADA218437, Simula, Inc. and U.S. Army Aviation Systems Command. Final Report, September 1986 – August 1989.
URL: <https://apps.dtic.mil/sti/tr/pdf/ADA218437.pdf>
- European Union Aviation Safety Agency (2020), *Certification Specifications and Acceptable Means of Compliance for Large Aeroplanes (CS-25)*, EASA. Accessed: 2025-06-16.
URL: <https://www.easa.europa.eu/en/document-library/certification-specifications/cs-25-large-aeroplanes>
- Facci, A. L., Ubertini, S. et al. (2015), ‘Numerical assessment of similitude parameters and dimensional analysis for water entry problems’, *Mathematical Problems in Engineering* **2015**.
- Faltinsen, O. M. (2005), *Hydrodynamics of high-speed marine vehicles*, Cambridge university press.
- Fan, X., Zhao, J., Qi, C., Wang, X. and Lyu, X. (2024), ‘On the water entry impact characteristics of high-speed vehicle with an arbitrary lagrangian-eulerian method’, *Applied Ocean Research* **150**, 104118.

- Federal Aviation Administration (2023), *Title 14 Code of Federal Regulations (CFR) Part 25 – Airworthiness Standards: Transport Category Airplanes*, FAA. Accessed: 2025-06-16.
URL: <https://www.ecfr.gov/current/title-14/chapter-I/subchapter-C/part-25/subpart-D/subject-group-ECFR88992669bab3b52/section-25.801>
- Feng, S., Wang, M., Wu, B. and Chao, H. (2020), The simulation of aircraft ditching based on ale method, *in* ‘IOP Conference Series: Materials Science and Engineering’, Vol. 926, IOP Publishing, p. 012019.
- Fontaine, E. and Tulin, M. (1998), On the prediction of nonlinear free-surface flows past slender hulls using 2d+ t theory: The evolution of an idea, *in* ‘RTO AVT symposium on fluid dynamic problems of vehicles operating near or in the air-sea interface, Amsterdam, The Netherlands’.
- Goron, M., Langrand, B., Jacques, N., Fourest, T., Tassin, A., Robert, A. and Chauveheid, D. (2023), ‘Simulation of water entry–exit problems highlighting suction phenomena by coupled eulerian–lagrangian approach’, *European Journal of Mechanics-B/Fluids* **100**, 37–51.
- Goron, M., Tassin, A., Langrand, B., Spinosa, E., Del Buono, A., Jacques, N., Fourest, T. and Iafrati, A. (2025), ‘Numerical simulation of the oblique water impact of double curvature bodies involving suction and cavitation phenomena’, *Journal of Fluids and Structures* **135**, 104322.
- Groenenboom, P., Cartwright, B. and McGuckin, D. (2021), ‘Recent features and industrial applications of the hybrid sph-fe method’, *International Journal of Computational Fluid Dynamics* **35**(1-2), 106–128.
- Groenenboom, P. H. and Cartwright, B. K. (2010), ‘Hydrodynamics and fluid-structure interaction by coupled sph-fe method’, *Journal of Hydraulic Research* **48**(sup1), 61–73.
- Groenenboom, P. and Siemann, M. (2015), ‘Fluid-structure interaction by the mixed sph-fe method with application to aircraft ditching’, *The International Journal of Multiphysics* **9**(3), 249–266.
- Guo, B., Liu, P., Qu, Q. and Wang, J. (2013), ‘Effect of pitch angle on initial stage of a transport airplane ditching’, *Chinese Journal of Aeronautics* **26**(1), 17–26.
- Huang, B., Qiu, S.-c., Li, X.-b., Wu, Q. and Wang, G.-y. (2019), ‘A review of transient flow structure and unsteady mechanism of cavitating flow’, *Journal of Hydrodynamics* **31**, 429–444.
- Hughes, K., Vignjevic, R., Campbell, J., De Vuyst, T., Djordjevic, N. and Papagiannis, L. (2013), ‘From aerospace to offshore: Bridging the numerical simulation gaps–simulation advancements for fluid structure interaction problems’, *International Journal of Impact Engineering* **61**, 48–63.
- Iafrati, A. (2015), Fluid-structure interaction during the high speed water entry of a plate, *in* ‘18th International Conference on Ships and Shipping Research, Lecco, Italy’.
- Iafrati, A. (2016), ‘Experimental investigation of the water entry of a rectangular plate at high horizontal velocity’, *Journal of Fluid Mechanics* **799**, 637–672.
- Iafrati, A. (2018), Effect of surface curvature on the hydrodynamics of water entry at high horizontal velocity, *in* ‘International Conference on Offshore Mechanics and Arctic Engineering’, Vol. 51302, American Society of Mechanical Engineers, p. V009T13A034.

- Iafrati, A. and Broglia, R. (2010), Comparisons between 2d+ t potential flow models and 3d rans for planing hull hydrodynamics, *in* ‘International Workshop on Water Waves and Floating Bodies, Harbin (China)’.
- Iafrati, A. and Grizzi, S. (2019), ‘Cavitation and ventilation modalities during ditching’, *Physics of Fluids* **31**(5), 052101.
- Iafrati, A., Grizzi, S. and Olivieri, F. (2020), ‘Experimental investigation of fluid–structure interaction phenomena during aircraft ditching’, *AIAA Journal* pp. 1–14.
- Iafrati, A., Grizzi, S., Siemann, M. and Montañés, L. B. (2015), ‘High-speed ditching of a flat plate: Experimental data and uncertainty assessment’, *Journal of Fluids and Structures* **55**, 501–525.
- Iafrati, A. and Korobkin, A. (2004), ‘Initial stage of flat plate impact onto liquid free surface’, *Physics of Fluids* **16**(7), 2214–2227.
- Iafrati, A. and Korobkin, A. (2008), ‘Hydrodynamic loads during early stage of flat plate impact onto water surface’, *Physics of Fluids* **20**(8), 082104.
- Judge, C., Troesch, A. and Perlin, M. (2004), ‘Initial water impact of a wedge at vertical and oblique angles’, *Journal of Engineering Mathematics* **48**, 279–303.
- Korobkin, A. (2004), ‘Analytical models of water impact’, *European Journal of Applied Mathematics* **15**(6), 821–838.
- Korobkin, A. A. and Scolan, Y.-M. (2006), ‘Three-dimensional theory of water impact. part 2. linearized wagner problem’, *Journal of Fluid Mechanics* **549**, 343–373.
- Krastev, V. K., Facci, A. L. and Ubertini, S. (2018), ‘Asymmetric water impact of a two dimensional wedge: A systematic numerical study with transition to ventilating flow conditions’, *Ocean Engineering* **147**, 386–398.
- Logvinovich, G. (1969), ‘Hydrodynamics of flows with free boundaries’, *Kyiv: Naukova Dumka* **215**.
- McBride, E. E. and Fisher, L. J. (1953), ‘Experimental investigation of the effect of rear-fuselage shape on ditching behavior’.
- Moghisi, M. and Squire, P. (1981), ‘An experimental investigation of the initial force of impact on a sphere striking a liquid surface’, *Journal of Fluid Mechanics* **108**, 133–146.
- Muñoz, C. L., Kohlgrüber, D. and Petsch, M. (2025), ‘High-fidelity aircraft simulations for the application in an industrialized ditching analysis process’, *AIAA Journal* pp. 1–6.
- Newman, J. N. (1971), *Marine hydrodynamics*, MIT press.
- Qu, Q., Hu, M., Guo, H., Liu, P. and Agarwal, R. K. (2015), ‘Study of ditching characteristics of transport aircraft by global moving mesh method’, *Journal of Aircraft* **52**(5), 1550–1558.
- Qu, Q., Liu, C., Liu, P., Guo, B. and Agarwal, R. K. (2016), ‘Numerical simulation of water-landing performance of a regional aircraft’, *Journal of Aircraft* **53**(6), 1680–1689.
- Riccardi, G. and Iafrati, A. (2004), ‘Water impact of an asymmetric floating wedge’, *Journal of engineering mathematics* **49**, 19–39.

- Schwarz, H., Überrück, M., Zemke, J.-P. M. and Rung, T. (2025), ‘Machine learning based prediction of ditching loads’, *AIAA journal* **63**(5), 1835–1854.
- Scolan, Y.-M. and Korobkin, A. A. (2001), ‘Three-dimensional theory of water impact. part 1. inverse wagner problem’, *Journal of Fluid Mechanics* **440**, 293–326.
- Seddon, C. and Moatamedi, M. (2006), ‘Review of water entry with applications to aerospace structures’, *International Journal of Impact Engineering* **32**(7), 1045–1067.
- Semenov, Y. A. and Iafrati, A. (2006), ‘On the nonlinear water entry problem of asymmetric wedges’, *Journal of Fluid Mechanics* **547**, 231–256.
- Siemann, M. and Langrand, B. (2017), ‘Coupled fluid-structure computational methods for aircraft ditching simulations: Comparison of ale-fe and sph-fe approaches’, *Computers & Structures* **188**, 95–108.
- Siemann, M., Schwinn, D., Scherer, J. and Kohlgrüber, D. (2018), ‘Advances in numerical ditching simulation of flexible aircraft models’, *International Journal of Crashworthiness* **23**(2), 236–251.
- Smiley, R. (1951), An experimental study of water-pressure distributions during landing and planing of a heavily loaded rectangular flate-plate model, Technical report, National Aeronautics and Space Administration, Washington, DC, USA.
- Smith, A., Warren, C. and Wright, D. (1957), *Investigations of the behaviour of aircraft when making a forced landing on water (ditching)*, Citeseer.
- Song, Z., Deng, R., Wu, T., Duan, X. and Ren, H. (2023), ‘Numerical simulation of planing motion and hydrodynamic performance of a seaplane in calm water and waves’, *Engineering Applications of Computational Fluid Mechanics* **17**(1), 2244028.
- Spinosa, E., Broglia, R. and Iafrati, A. (2022), ‘Hydrodynamic analysis of the water landing phase of aircraft fuselages at constant speed and fixed attitude’, *Aerospace Science and Technology* **130**, 107846.
- Spinosa, E. and Iafrati, A. (2021), ‘Experimental investigation of the fluid-structure interaction during the water impact of thin aluminium plates at high horizontal speed’, *International Journal of Impact Engineering* **147**, 103673.
- Streckwall, H., Lindenau, O. and Bensch, L. (2007), ‘Aircraft ditching: a free surface/free motion problem’, *Archives of civil and mechanical engineering* **7**(3), 177–190.
- Sun, H. and Faltinsen, O. M. (2011), ‘Dynamic motions of planing vessels in head seas’, *Journal of marine science and technology* **16**, 168–180.
- Tassin, A., Jacques, N., Alaoui, A., Nême, A. and Leblé, B. (2010), ‘Assessment and comparison of several analytical models of water impact’, *The International Journal of Multiphysics* **4**(2), 125–140.
- Tassin, A., Piro, D., Korobkin, A., Maki, K. and Cooker, M. (2013), ‘Two-dimensional water entry and exit of a body whose shape varies in time’, *Journal of Fluids and Structures* **40**, 317–336.

- Van Nuffel, D., Vepa, K., De Baere, I., Degrieck, J., De Rouck, J. and Van Paepegem, W. (2013), ‘Study on the parameters influencing the accuracy and reproducibility of dynamic pressure measurements at the surface of a rigid body during water impact’, *Experimental mechanics* **53**(2), 131–144.
- Von Karman, T. (1929), The impact on seaplane floats during landing, Technical Report 321, National Advisory Committee for Aeronautics.
- Wagner, H. (1932), ‘Über stoß-und gleitvorgänge an der oberfläche von flüssigkeiten’, *ZAMM-Journal of Applied Mathematics and Mechanics/Zeitschrift für Angewandte Mathematik und Mechanik* **12**(4), 193–215.
- Wang, B., Nie, L. and Ren, Y. (2024), ‘Numerical simulation of different aircraft sub-floor structures during ditching’, *The Aeronautical Journal* **128**(1329), 2530–2544.
- Wang, G., Senocak, I., Shyy, W., Ikohagi, T. and Cao, S. (2001), ‘Dynamics of attached turbulent cavitating flows’, *Progress in Aerospace sciences* **37**(6), 551–581.
- Wang, H. (2023), Dynamic simulation of civil aircraft ditching based on cfd, in ‘2023 3rd International Conference on Electrical Engineering and Control Science (IC2ECS)’, IEEE, pp. 1236–1239.
- Wenli, L., Weibin, G. et al. (2025), ‘Experimental investigation of dynamic characteristic during civil aircraft ditching’, *Chinese Journal of Aeronautics* **38**(4), 103281.
- Xu, G., Duan, W. and Wu, G. (2008), ‘Numerical simulation of oblique water entry of an asymmetrical wedge’, *Ocean Engineering* **35**(16), 1597–1603.
- Zha, R., Wang, K., Sun, J., Tu, H. and Hu, Q. (2024), ‘Numerical simulations of seaplane ditching on calm water and uniform water current coupled with wind’, *Journal of Marine Science and Engineering* **12**(2), 296.
- Zhang, T., Li, S. and Dai, H. (2012), ‘The suction force effect analysis of large civil aircraft ditching’, *Science China Technological Sciences* **55**(10), 2789–2797.
- Zhao, R. and Faltinsen, O. (1993), ‘Water entry of two-dimensional bodies’, *Journal of fluid mechanics* **246**, 593–612.
- Zheng, Y., Qu, Q., Liu, P., Hu, T., Shi, X. and Zhou, P. (2025), ‘Numerical analysis of impact loads on a two-dimensional flat plate during ditching’, *Physical Review Fluids* **10**(4), 044801.
- Zheng, Y., Qu, Q., Liu, P., Wen, X. and Zhang, Z. (2021), ‘Numerical analysis of the porpoising motion of a blended wing body aircraft during ditching’, *Aerospace Science and Technology* **119**, 107131.